UNIVERSITY OF BIRMINGHAM

High performance cooling of a HVDC converter using a fatty acid ester-based phase change dispersion in a heat sink with double-layer oblique-crossed ribs

Li, Qi; Fischer, Ludger; Qiao, Geng; Mura, Ernesto; Li, Chuan; Ding, Yulong

Link to publication on Research at Birmingham portal

INTERNATIONAL JOURNAL OF
ENERGY RESEARCH WILEY

High performance cooling of a HVDC converter using a fatty acid ester-based phase change dispersion in a heat sink with double-layer oblique-crossed ribs

Qi Li[1] | Ludger Fischer[2] | Geng Qiao[3] | Ernesto Mura[3] | Chuan Li[1] | Yulong Ding[1]

[1]Birmingham Centre for Energy Storage (BCES) & School of Chemical Engineering, University of Birmingham, Birmingham, UK

[2]Lucerne University of Applied Sciences and Arts, Horw, Switzerland

[3]Global Energy Interconnection Research Institute Europe GmbH, Berlin, Germany

Correspondence
Chuan Li and Yulong Ding, Birmingham Centre for Energy Storage (BCES) & School of Chemical Engineering, University of Birmingham, UK B15 2TT.
Email: c.li.4@bham.ac.uk (C. L.) and y.ding@bham.ac.uk (Y. D.)

Summary

The paper concerns with a high performance cooling method for a HVDC converter using fatty acid ester-based phase change dispersion (PCD) in a heat sink with double-layer oblique-crossed ribs. Thermo-physical properties of PCDs were first characterized under both solid and liquid states, and the cooling performance of the heat exchanger was then experimentally examined, by heating two copper blocks clamped closely to the aluminium heating surfaces. A three-dimensional Euler-Euler multiphase approach was further performed to evaluate the thermal performance under different operating conditions including heating power, flowrate and PCD concentration. The results showed that the viscosity of PCD can be a 100 times that of water, but the increased pumping power was only ~17.01% on average. The use of the PCD achieved a lower temperature of heat sink and fluid than that of water under the same set of conditions due to the latent heat of the PCM, thus enabling a safer and cooler environment for temperature-sensitive HVDC components such as insulated gate bipolar transistors (IGBT). An optimal set of working conditions was proposed and a flowrate of 8 L/min under a heating power of 1.1 kW and a PCM concentration of 25% was recommended for industrial cooling operations.

Highlights

- A novel cooling method for HVDC converter using a fatty acid based PCD presented.
- A 3D Euler-Euler modelling performed and compared with experiments.
- Effects of operating conditions and PCM loading on cooling behaviour discussed.
- Three calculating methods of heat transfer coefficients compared.
- Optimal PCD cooling condition given based on overall performance evaluation.

KEYWORDS
Euler-Euler multiphase modelling, fatty acid ester, HVDC converter cooling, multi-stream heat sink, oblique-crossed ribs, phase change dispersion

1 | INTRODUCTION

Rapid growing demand for electric power and continuous effort of miniaturization of high-voltage direct current (HVDC) devices drive heat flux to the megawatt range.[1,2] In a high power transmission system, devices such as HVDC converters that transform alternating current (AC) to direct current (DC) and vice versa via controllable electric switches, high power dissipation can be up to 9.72 kW, which is nearly 30% of the total HVDC power loss.[3,4] Under such a high dissipation, sensitive power semiconductor devices such as insulated gate bipolar transistor (IGBT) in the HVDC converter could experience a heat flux over 2 MW/m[25] and a temperature increase to 90°C,[6] depending on the source voltage and switching frequency. This could lead to system thermal runaway because silicon as workhorse material could not bear the crucial operational conditions.[7] To avoid the thermal runaway, new semiconductor materials such as SiC or GaN have been developed.[7,8] However, applications of such materials are limited by available power module packages,[9] package agents,[10] peripheral components[11] and economic considerations. Moreover, persistent heat still generates in the presence of new material because multiple processing by power electronics converters before the end use. These reasons push the rapid development of novel thermal management technologies. Additionally the smaller the heat sinks leads to a higher volumetric power density,[12] which requires a more advanced and efficient cooling method.

The two most commonly used technologies in cooling electronic devices are air cooling and water cooling. The air based cooling systems, classified as natural or forced air flux by the way air flows, are normally suffice for lower power electronic devices with a power dissipation rate below ~1500 W.[13] The introduction of a liquid but water, which is often a dielectric, a high cooling efficiency or lower/stabilized temperature can be achieved. Among various coolants, phase change material (PCM) offers more isothermal operation through storing heat at a high energy density within a small temperature change.[14-18] Further thermal performance enhancements can be realized by dispersing and transporting PCM in a thermally active fluid that is immiscible with the PCM, the so-called phase change dispersion (PCD). An incredible number of PCM slurries have been developed by combining various proportions of PCMs, modifiers, nucleation agents, etc. This allows customizing thermal-physical properties with an adaptability that is hardly possible for other class of solvents. Under a targeted set of operational conditions, the PCD can be designed to enhance thermal performance of heat sink with a uniform temperature distribution and a small temperature change.[19-22]

To ensure long-term lifespan in a high voltage environment, the PCD component is best to be electrically insulating for cooling HVDC converters. As a type of organic dielectric material, paraffin wax have been widely used as PCM due to the widely studied interaction between paraffin and classical emulsifier.[23-25] However, paraffin often yields different crystalline phases during phase change, which may result in contamination on the wall of heat exchanger and require strong solvents for cleaning at a high temperature. The low thermal conductivity, unpleasant odour and flammability make them even harder for industrial applications. The long-chain fatty acid ester from renewable sources offers an alternative PCM to paraffin.[26] Such a material normally works in the ambient-to-moderate temperature range[27] (20-100°C), which is suitable for HVDC electronic devices cooling[28] (around 60°C). PCD emulsles are often fabricated in a high energy environment provided by a high-shear mixer or an ultrasound generator. The multiphase suspension shows Newtonian behaviour at low emulsion concentrations, but becomes highly non-Newtonian at an emulsion concentration, with a clear demarcation hard to be determined empirically. For example, a 30 w/w % tetradecane emulsion[29] was found to be Newtonian, whereas a paraffin/water emulsion[30] showed pseudo-plastic behaviour with a mass fraction between 15% and 50%. The viscosity of emulsions can be 2-550 times that of water,[31,32] yet the pressure drop has been found not as big as the viscosity increase and hence a small increase in the pumping work.[33,34] As a result, a detailed material characterization of the PCD under both solid and liquid conditions of the PCM is required to enable an accurate prediction of thermal performance of the heat sink using PCDs.

The relative low thermal conductivity of the organic PCD reduces the cooling efficacy, leading to challenges in enhancing and optimizing the thermal management of PCD based heat sinks.[35] A great deal of efforts has been devoted to the design of enhanced heat transfer surfaces to lower the convective heat transfer resistance.[36] An introduction of a large number of fins in the cross-sectional direction can reduce the thermal and hydraulic boundary layers, leading to higher temperature and velocity gradients at the wetted wall for an efficient removal of thermal energy.[29] Similarly the use of metal foams could enhance heat transfer.[37] However, a significant increase in the pressure drop may offset the enhanced heat transfer by an increase in the pumping power. Chai et al.[38] studied the heat transfer in microchannel containing offset ribs, with rectangular, backward triangular, isosceles triangular, forward triangular and semicircular shapes. Kanargi et al.[39] introduced the cross-connected alternating converging-diverging channel heat sink to disrupt boundary layers and

showed a decreased junction temperature up to 5 K for a 40 W heating power with air cooling, but the fanning friction factor was 19 times higher than a straight channel at high Re numbers. In industrial practical applications, the series and parallel arrangement of heat sinks can amplify the increased pressure drop. To avoid unnecessary energy consumption but keep the advantage of thermal performance enhancement, a multi-stream plate heat exchanger can be used due to compact structure, high efficiency, low cost and ease of handling multiple streams.[40-42] Radwan et al.[43] developed a monolithic double-layer microchannel heat sink for concentrated photovoltaic cooling under parallel and counter flows, and found a single-phase-liquid parallel flow could effectively cool the PV at a higher flowrate.

Metals such as aluminium alloys and copper are widely used to manufacture heat sinks, due to their light-weight and high thermal conductivity.[44-46] In the evaluation of heat sink performance, heat transfer across a contact intermediate formed by any two solid surfaces is accompanied by a measurable temperature drop, because there exist interfacial thermal contact resistance (ITCR) to heat flows. The ITCR is caused by the imperfect heat transfer surfaces at the joint, which only give a small fraction of the apparent contact area while rest is filled with air or other media. The complex geometrical and thermo-physical parameters in such a case depend on many factors, such as surface micro-topography, micro-hardness, contact pressure, temperature level of the interface, solid thermal conductivities and type of substance in the interstitial gaps. The ITCR between aluminium alloys and copper has received lots of attention due to their wide use in practical applications. Yüncü[47] found that the thermal contact conductance of Al–Cu varies between 10.3 and 30.88 kW/(m^2 K), depending on the contact pressure and micro-hardness. Shi et al.[48] evaluated the influence of temperature on ITCR between aluminium nitride and copper at cryogenic conditions. The ITCR was found to decrease with increasing interface temperature and contact pressure, and ranging between 5×10^{-4} and 3×10^{-3} m^2·W/K. Depending on the contact surface condition, the thermal conductance of ground and milled Al–Cu was found to be 42-56 kW/(m^2 K) and 12-22 kW/(m^2 K),[49] respectively.

Due to the complexity of performing local concentration and velocity measurements of PCD in an insulated pipe, numerical simulations have therefore been widely used for the study. In particular, the Euler-Euler model has been shown to be a fruitful approach to dealing with two-phase mixtures. Göktepe et al.[50] compared Eulerian-Eulerian and Eulerian-mixture model to study heat transfer coefficients and friction factors, and recommended the former for description of the two-phase interaction. Wang et al.[51] studied ice slurry (<25 v/v %) in horizontal, vertical and 90° elbow pipes using the Euler-Euler model, and found a relative errors of ±20% with respect to the measurements. Ma et al.[20] investigated the hydraulic and heat transfer characteristics of PCD in a circular smooth pipe using the Euler-Euler model, and showed a good agreement with previous experimental results. However, the use of the Eulerian-Eulerian model to study heat sinks is still limited due to large computation resource demand. Another noteworthy fact of heat sink is that there is still lack of unified standard of temperatures used for heat transfer coefficient calculation. The wall temperature can either be derived from wetted wall or outer wall of the heat sink, and the fluid temperature is either the bulk mean temperature or average value between inlet and outlet. The temperature difference used to drive the convective heat transfer coefficient can be calculated by taking the difference between the wall and fluid temperature,[36,52] or from log mean temperature difference.[53,54] A large deviation between the two can occur at small temperature differences under a high heat flux. Thus, an accurate and more convenient calculation method is needed.

In this work, an electrically insulting fatty acid ester-based PCD is used for efficient HVDC converter cooling through a heat exchanger with double-layer oblique-crossed ribs. The PCD was characterized and the heat transfer performance of the heat exchanger was experimentally examined, by heating two copper blocks clamped closely to the aluminium heating surfaces. Such a device is able to disrupt thermal and hydraulic boundary layers, providing a higher temperature gradient near the wall and rapid removal of thermal energy. A 3D Euler-Euler multiphase approach was then used to model the PCD cooling performance under different heating powers, flowrates and PCD concentrations. The complex geometry of heat sink brings about difficulties in the evaluation of heat transfer coefficient, thus three analysis methods based on temperatures of the heating wall, the wetted wall and the inlet/outlet fluid were compared. An optimal set of working conditions was proposed and recommended for industrial cooling operations. The present work provides a high-performance and economic cooling method, using a novel coolant inside a heat sink with interrupted hydraulic and thermal boundary layers.

2 | EXPERIMENTAL

2.1 | PCD preparation and properties measurements

To meet the cooling requirements of a HVDC converter, the PCD should have low electrical conductivity to

ensure safety with a long lifespan in a high voltage environment and a high heat flux over a temperature range of ~320.65-323.15 K. The melting range of the target PCM should align with the temperature range, taking into account the effect of the emulsifier for producing the emulsion (PCD). An extensive screening and formulation exercise was performed to produce the PCD using deionised water and a mixture of commercial fatty acid esters based PCM (50 w/w % Crodatherm 53 + 50 w/w % Crodatherm 47, Croda International PLC, UK). An emulsifier, consisting of a long chain and a short chain ethoxylated fatty alcohols (75 w/w % Steareth-100 + 25 w/w % Steareth-2, KLK Oleo, Germany), and a small portion (1.6 w/w %) of glycerol, were added to the formulation to ensure the PCD stability. An optimal PCD was found to be containing 16 w/w % of PCM, 4 w/w % of emulsifier, 0.5 w/w % nucleation agents in continuous phase, which was used in this work. The dispersion was manufactured by dispersing PCM phase into deionized water using a Polytron 10-35 GT lab rotor-stator at the Lucerne University of Applied Sciences and Arts, Switzerland.

The thermo-physical properties of PCD were measured at the Birmingham Centre for Energy Storage (BCES) of the University of Birmingham. Table 1 summarizes the results. Each measurement was repeated at least three times to ensure reproducibility. The solution density was measured using an Anton-Paar DMA 4100 M density meter (UK). The thermal conductivity was derived from laser flash measurements with a Netzsch LFA 427 (Netzsch, German).[55] The specific heat capacity, melting point and phase change enthalpy of melting were determined using a DSC (Differential Scanning Calorimeter, DSC2, Mettler Toledo, USA). The specific heat data are shown in Figure 1 for different PCDs with a PCM volume fraction (ϕ) between 5% and 25%. One can see that the emulsifier is also a PCM, which is therefore multifunctional in this application. The PCD stability against creaming, sedimentation and coalescence was also studied by an optical centrifuge of LUMiSizer, and the results demonstrated the sufficient stability of the proposed PCD even experienced more than 200 cycling times.

The rheological behaviour of PCD was measured with a rotational MCR 502 rheometer (Anton Paar, UK). The influences of shear rate and temperature on PCM and emulsifier viscosities are illustrated in Figure 2A. At a shear rate lower than ~25 seconds^{-1}, an irregular fluctuation of the viscosity occurs mainly due to low torque

TABLE 1 Thermo-physical properties of water, PCM and PCD under both solid and liquid status of the PCM

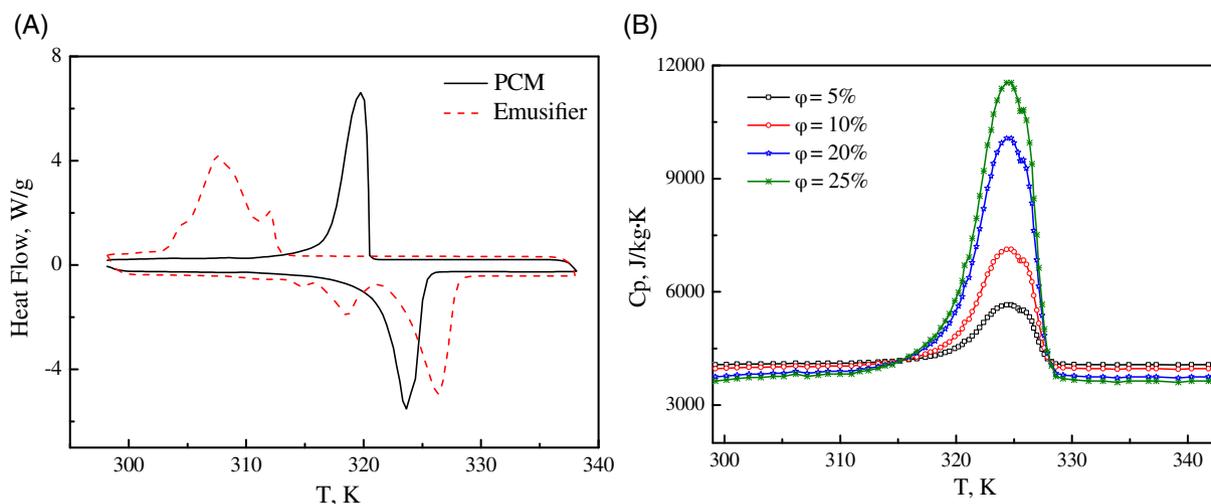|	ρ [kg/m^3]		k [W/(m K)]		c_p [kJ/(kg K)]		T_{melt} [°C]	Δh_{pc} [kJ/kg]
Working Temperature [K]	**298.15**	**328.15**	**298.15**	**328.15**	**298.15**	**328.15**	**-**	**-**
Water	998.2	988.4	0.61	0.651	4.18	4.18	-	-
PCM	902	827.2	0.231	0.206	2.78	2.38	47.13	193.38
Emulsifier	1011.4	1005.3	0.293	0.301	2.28	2.21	49.72	141.53
PCD	983.9	980.5	0.529	0.561	3.82	3.78	50.95	26.11

FIGURE 1   A, DSC measurement of PCM and emulsifier, and B, Cp variation with temperature of different PCM concentration, ϕ = 5%, 10%, 20% and 25% [Colour figure can be viewed at wileyonlinelibrary.com]
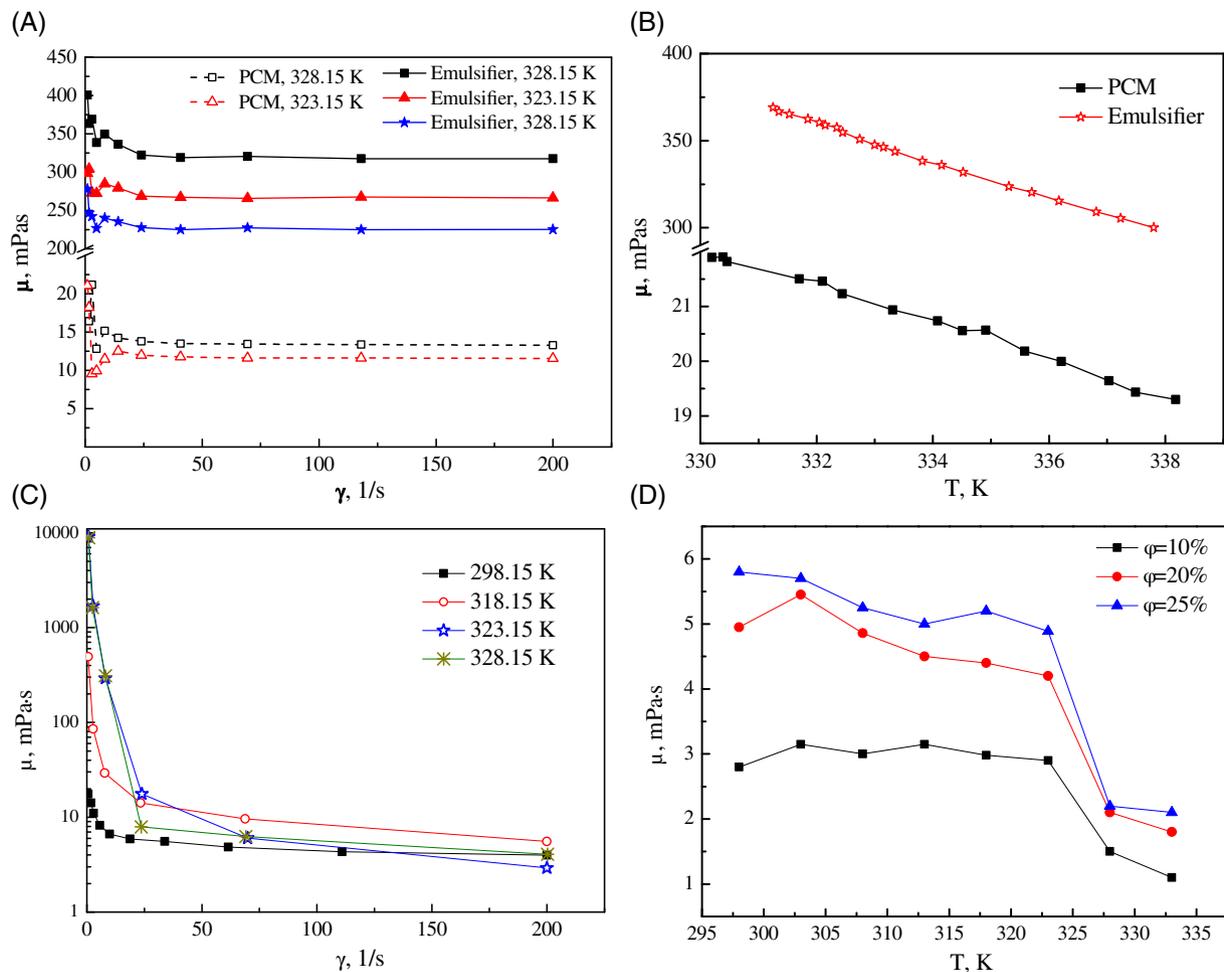
FIGURE 2   A, Rheology behaviour of pure PCM and emulsifier under various shear rates and temperature; B, temperature dependence of viscosity at a shear rate of 100 seconds^{-1}; C, rheological behaviour of PCD under various shear rates and temperatures with $\phi = 20\%$; and D, temperature dependence of viscosity of the PCD at $\gamma = 100\ s^{-1}$ [Colour figure can be viewed at wileyonlinelibrary.com]

resolution.[56,57] An increase in the shear rate to ~25 seconds^{-1} leads to the viscosity of almost constant for a given temperature, exhibiting the Newtonian behaviour. Such a rheological behaviour is also confirmed by the linear relationship between viscosity and temperature under a constant shear rate of 100 seconds^{-1} (Figure 2B). Figure 2A and B also indicate that viscosity of the emulsifier is significantly higher than that of PCM by a factor of 20.

Unlike the PCM and the emulsifier, the rheological behaviour of the PCD follows a non-Newtonian characteristic, as shown in Figure 2A and B. With increasing shear rate, the PCD viscosity decreases regardless of the PCM at the solid or liquid status, and the viscosity of the PCD can reach up to 10 000 mPa·s at a shear rate below ~ < 25 seconds^{-1} even when PCD is melted (323.15 K and 328.15 K); see Figure 2C. Increasing the PCM concentration increases the PCD viscosity (Figure 2D). The PCD viscosity is lower when the PCM is at the liquid status as shown in Figure 2D, but the decrease is rather smaller compared to the low shear rate values.

The size distribution of the PCD was measured using the dynamic light scattering method with a Zetasizer Nano-ZS (Malvern, UK) in BCES of University of Birmingham, and the results are shown in Figure 3. The particle size distribution could be fitted by the Rosin-Rammler (R-R) distribution (given in the inset), $Y_d = e^{-\left(d/\bar{d}\right)^n}$, with Y_d the cumulative PCD volume fraction having a diameter larger than d; n = 1.276 the size distribution parameter; $\bar{d} = 3.0\ \mu m$ the particle size and size constant; and $dp_{min} = 0.065\ \mu m$ and $dp_{max} = 6.5\ \mu m$, corresponding to 99.9% and 0.1% of the cumulative fraction for the R-R distribution,[58] respectively. The average deviation between the measurements and fitted correlation is 12.89%.

2.2 | Experimental rig of cooling performance measurements

The performance of the PCD for the HVDC converter cooling was performed by using a heat sink with double-
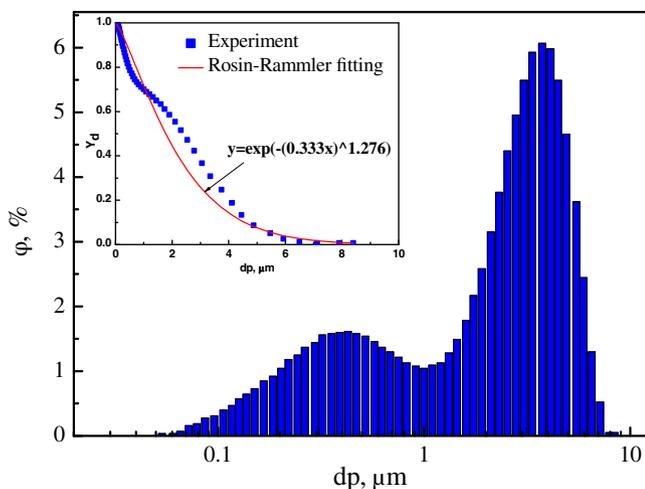
FIGURE 3 Relationship between particle volume fraction and particle diameter. Inset shows the fitting of Rosin–Rammler distribution [Colour figure can be viewed at wileyonlinelibrary.com]

layer oblique-crossed ribs, manufactured by Mersen Co Ltd, Shanghai. The heat sink was made of AlMgSi0.5, which has heat and electrical conductivities of 185 W/ (m K) and 28.6×10^6 S/m, respectively. Figure 4A shows a snapshot of the heat sink. Two identical circular heating surfaces with a diameter of 135 mm were made in close contact with the top and bottom surfaces of the heat sink. The cooling section was formed by overlapping two web layers within the heat sink to increase the heat transfer area and fluid turbulence. The angle between the ribs of upper and bottom layer was 30°. The fluid channel was formed between the rib gaps with a cross-section dimension of 3.6 mm (W_c) × 4 mm (H_c) and porosity of 0.576. The cooling fluid was pumped into the circular inlet (internal diameter, ID, = 9 mm), exchanging heat with the cooling section before exiting at the outlet (with the same ID as the inlet). The cooling section had width of 130 mm and length (refers to the distance between inlet and outlet centre) of 118 mm.

The cooling experiment was conducted at Lucerne University of Applied Science and Arts (Switzerland). The circular heating surfaces were provided by two copper blocks powered by electrical heating as shown in Figure 4B. The blocks and the heating surfaces of the heat sink were tightly clamped by torque wrenches. Each block was equipped with six heating cartridges so that a constant heat flux boundary condition can be maintained, to simulate the power dissipation of a HVDC converter thyristor. The maximum heating power per cartridge was 200 W, giving a total power of 1.5 kW per side. All 12 cartridges were powered by a thyristor power controller (TYA-201, JUMO Co Ltd, UK), allowing a precise regulation of the heat input with an uncertainty of ± 0.02 P_{el} (P_{el} is the electrical power). At a distance of 2.5 mm from the interface, four

PT100 1/3 DIN wire sensors (Roth +Co AG, Switzerland) were placed to measure the temperatures of one of the blocks with a measurement uncertainty less than ± 0.1 K; see late for more details. The heating section was thermally insulated by an aluminium foil together with PIR shells (Swisspor, Switzerland). The pressure drop was measured by a Deltabar S PMD75 device (Endress + Hauser, Switzerland), with a range of 0-40 bar and an accuracy of 0.075%.

Figure 4C illustrates a schematic of the experimental rig. The fluid was driven by an impeller pump (Zuwa NIROSTAR/V 2000-B/PT, Germany) into the system. A Coriolis flow meter (Promass F83, Endress + Hauser AG, Switzerland) and a by-pass valve were used to control the mass flowrate of the flow with an uncertainty of ± 0.004 $\dot{m}$, where $\dot{m}$ is the mass flow rate. To ensure a stable and safe operation in the electrical environment, the PCD went through a deionization unit filled with a resin, Amberjet UP 6150, purchased from Rohm & Haas, USA. A nylon filter with a mesh size of 200 μm was used to remove any unwanted impurity before the PCD entering the system. To remove the heat added to the fluid in the heat section for recirculation, a thermostat (TYA-201, JUMO Co Ltd, UK) was used to cool the fluid before re-entering the testing rig. All measurements were recorded at the steady state (often reached after ~10 minutes operation). To determine heat loss of the system, the setup was first tested with water under various $\dot{m}$ and P_{el}. The heat loss, identified as the difference between P_{el} and water heating from inlet to outlet $Q_{loss} = P_{el} - \dot{m}\left(C_p T_{out} - C_p T_{in}\right)$, was found to be 20 W on average, which was used for the PCD calculations.

2.3 | Data analysis

Temperatures measured by T03 to T06 (Figure 4C) were from the copper block side rather than from the heat sink. To accurately describe the thermal performance of the heat sink, thermal resistance within the copper (R_{th1}) and ITCR between the aluminium heat sink and copper block (R_{th2}) should be estimated, as illustrated in Figure 4D. The copper resistance is a function of thermal conductivity, k, distance, s, and heating area, A:

$$R_{th1} = s/kA \quad (1)$$

which yields a constant value of 4.48×10^{-4} K/W. The relationship between ITCR and thermal conductance (h_j) is defined as

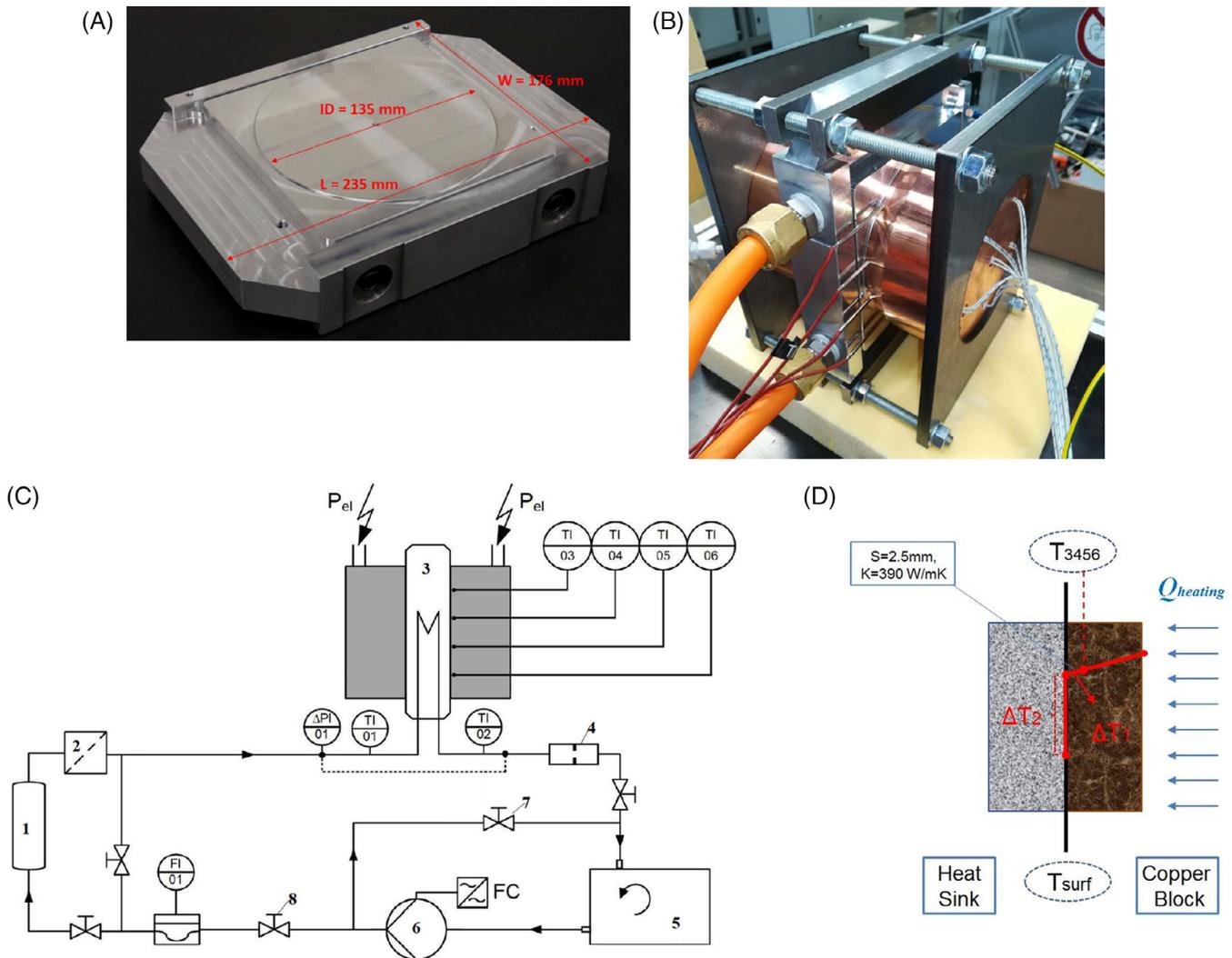$$R_{th2} = \frac{1}{h_j A} \quad (2)$$

FIGURE 4 A, A snapshot of the heat sink, B, a snapshot of the heating section, C, a schematic diagram of the experimental rig (1 – Deionisation; 2 – Filter; 3 – Converter; 4 – Re-dispersion unit; 5 – Re-cooling unit; 6 – Pump; 7 – By-pass valve; 8 – Throttle valve), and D, schematic of the thermal resistance between heating surface and copper block [Colour figure can be viewed at wileyonlinelibrary.com]

Since both metal surfaces were planar and finely polished, the thermal conductance was chosen as $h_j = 12\text{-}22$ kW/(m^2 K). This gives to R_{th2} a range between 3.18×10^{-3} K/W and 5.82×10^{-3} K/W for the present work. The temperature difference between heating surface and T_{3456} (as shown in Figure 4D) can thus be determined by $\Delta T = P(R_{th1} + R_{th2})$, where P is the heating power.

The measurement uncertainty is defined as the uncertainty of a derived parameter, X, caused by the uncertainties of individual measured variables, can be calculated by the following expression[43]:

$$\omega_X = \left(\frac{\partial X}{\partial x_1}\right)^2 \omega_{X1}^2 + \left(\frac{\partial X}{\partial x_2}\right)^2 \omega_{X2}^2 + \dots + \left(\frac{\partial X}{\partial x_n}\right)^2 \omega_{Xn}^2 \quad (3)$$

where ω_X is the uncertainty of variable X and ω_{Xn} is the uncertainty of parameter x_n. The maximum uncertainty of temperature derived is therefore ± 0.35 K.

3 | MATHEMATIC MODELLING

3.1 | Mathematical model

With the Euler-Euler method, the PCM particles and glycerol-water solution are treated as interpenetrative continua, coupled through the interphase momentum and heat balance. The PCD is assumed to be incompressible and in the turbulent flow regime, and the PCM particles are assumed to be smooth, inelastic and spherical during phase change. Compared to the Eulerian-Lagrangian method

where the equation of motion is solved for each of particles, the Euler granular model solves only one conservation equation for the solid phase. Thus it can be used for concentrated fluid in a relative large computational domain. The k-ω turbulence model with shear stress transport (SST) model was adopted, which uses the k-ε model in the core of the flow and switches to the k-ω model in the near-wall regions. The rationale for the use of such a model lies in their proven accuracies in solving mixture problems in the near-wall region.[59,60] The detailed turbulence kinetic energy and specific dissipation rate can be referred to Menter.[61]

- Continuity equation for i[th] phase:

$$\frac{\partial}{\partial t}(\alpha_i \rho_i) + \nabla \cdot \left(\alpha_i \rho_i \vec{v}_i\right) = 0 \tag{4}$$

where the subscript i = l, s, representing the liquid phase or solid phase, respectively; α, ρ and $\vec{v}$ denote respectively the volume concentration, density and velocity of the different phase.

- Momentum conservation equation:

$$\frac{\partial}{\partial t}\left(\alpha_i \rho_i \vec{v}_i\right) + \nabla \cdot \left(\alpha_i \rho_i \vec{v}_i \vec{v}_i\right) = -\alpha_i \nabla P + \nabla$$
$$\cdot \bar{\bar{\tau}}_i + \alpha_i \rho_i \vec{g} + \vec{F}_D + \vec{F}_L + \vec{F}_{td} + \vec{F}_{VM} \tag{5}$$

where $\bar{\bar{\tau}}_l$ represents the stress-strain tensor of the ith phase:

$$\bar{\bar{\tau}}_i = \alpha_i \mu_i \left[\nabla \vec{v}_i + \left(\nabla \vec{v}_i\right)^T - \left(\frac{\zeta_i}{\mu_i} - \frac{2}{3}\right)\nabla \cdot \vec{v}_i \vec{I}\right] \tag{6}$$

where μ_i, ζ_i and $\vec{I}$ are the shear viscosity, bulk viscosity and unit vector, respectively; $\vec{F}_{D,l}$, $\vec{F}_{L,l}$, $\vec{F}_{td,l}$, $\vec{F}_{VM}$ are respectively the drag force, lift force, turbulent dispersion force and virtual mass force between the two phases. The solid phase bulk viscosity, ζ_s, and shear viscosity, μ_s, are given by Lun et al.[62] and Syamlal and O'Brien,[63] respectively:

$$\zeta_s = \frac{4\alpha_s \rho_s d g_0 (1+e_{ss})\sqrt{\theta_s}}{3\sqrt{\pi}} \tag{7}$$

$$\mu_s = \frac{4\alpha_s \rho_s d(1+e_{ss})g_0\sqrt{\theta_s}}{5\sqrt{\pi}} + \frac{10\rho_s d\sqrt{\pi\theta_s}}{96\alpha_s(1+e_{ss})g_0}\left[1+\frac{4(1+e_{ss})g_0\alpha_s}{5}\right]^2 \tag{8}$$

where e_{ss} is the particle–particle restitution coefficient and chosen to be 0.9; θ_s is the granular

temperature; and g_0 is the radial distribution function defined as[64]:

$$g_0 = \left[1 - (\alpha_s/\alpha_{s,max})^{1/3}\right]^{-1} \tag{9}$$

where $\alpha_{s,\,max}$ is the maximum packing fraction and equals to 0.62 for monodisperse spheres.[65] The granular temperature θ_s is used to describe the fluctuating particle motion, derived from the fluctuating energy balance equation as follows:

$$\frac{3}{2}\left[\frac{\partial}{\partial t}(\alpha_s\rho_s\theta_s) + \nabla \cdot \left(\alpha_s\rho_s\vec{v}_s\theta_s\right)\right]$$
$$= \left(\bar{\bar{\tau}}_s - P_s\bar{\bar{I}}\right)\cdot\nabla\vec{v}_s + \nabla\cdot(k_{\theta_s}\nabla\theta_s) + \varphi_{sl} - \gamma_{\theta_s} \tag{10}$$

where k_{θ_s}, φ_{sl} and γ_{θ_s} represent the diffusion coefficient, interphase energy exchange and collisional dissipation of energy, respectively. The solid pressure, P_s, follows the work of Gidaspow[66] and given by:

$$P_s = \alpha_s\rho_s\theta_s[1 + 2g_0\alpha_s(1+e_{ss})] \tag{11}$$

The granular temperature at the inlet is given by[67]:

$$T_s = 0.004(U_s)^2 \tag{12}$$

Among the interfacial forces, the dominate drag force is described by Syamlal and O'Brien[63] model which takes the following form:

$$\vec{F}_D = \frac{C_D Re_s \alpha_l}{24v_s^2} \tag{13}$$

where C_D is the drag force coefficient expressed as:

$$C_D = \left(0.63 + \frac{4.8}{\sqrt{Re_s/v_s}}\right)^2 \tag{14}$$

A virtual mass would occur when the solid phase accelerates relative to the carrier phases. The inertia of the carrier-phase mass encountered by the accelerating particles exerts the virtual mass force on particles, given as:

$$\vec{F}_{VM} = 0.5\alpha_s\rho_l\left(\frac{d_l\vec{v}_l - d_s\vec{v}_s}{dt}\right) \tag{15}$$

In a non-uniform or swirling flow, the dispersed particles experience a lift force perpendicular to the relative velocity vector[68]:

$$\vec{F}_{L,l} = \frac{2C_L v^{0.5} \rho d_{ij}}{\rho_s d(d_{lk} d_{kl})^{0.25}} \left| \vec{v}_s - \vec{v}_l \right| \tag{16}$$

where C_L is the lift force coefficient and taken as 0.25 for a spherical particle. The particle distribution is dominated by the turbulent dispersion force when the size of turbulent eddies are larger than the particle size[69]:

$$\vec{F}_{td,1} = C_{td} \gamma_{sl} \frac{\mu_{t,1}}{\sigma_{sl}} \left(\frac{\nabla \alpha_s}{\alpha_s} - \frac{\nabla \alpha_l}{\alpha_l} \right) \tag{17}$$

where C_{td} is the dispersion coefficient and determined to be 1. The energy conservation equation for i[th] phase can be formulated as:

$$\frac{\partial}{\partial t}(\alpha_i \rho_i H_i) + \nabla \cdot \left(\alpha_i \rho_i \vec{v}_i H_i \right) = \nabla \cdot (\lambda_{e,i} \nabla T_i) + \bar{\bar{\tau}}_i$$
$$\cdot \vec{v}_i - h_{sl}(T_i - T_q) \tag{18}$$

where h_{sl} is the particle–liquid heat transfer coefficient and given by[70]:

$$h_{sl} = \frac{6\alpha_s \lambda_l}{d^2} \Big[(7 + 10\alpha_l + 5\alpha_l^2)(1 + 0.7 Re_s^{0.2} Pr^{1/3})$$
$$+ (1.33 - 2.4\alpha_l + 1.2\alpha_l^2) Re_s^{0.7} Pr^{1/3} \Big] \tag{19}$$

The effective thermal conductivities in the main flow and near-wall regions have been given by Zehner and Schlünder[71] and Legawiec and Ziólkowski,[72] respectively. In the near-wall region, no slip boundary is assumed for the liquid phase while a partial slip boundary is assumed for solid phase following Johnson-Jackson equations[73] with the shear force given as:

$$\tau_{sw} = -\frac{\sqrt{3}\rho_s g_0 \alpha_s \varphi \sqrt{\theta_s} \vec{\nu}_{sw}}{6\alpha_{s,max}} \tag{20}$$

and the fluctuating energy expressed by:

$$q_{sw} = \frac{\sqrt{3}\rho_s g_0 \alpha_s \varphi \sqrt{\theta_s} \vec{\nu}_{sw} \vec{\nu}_{sw}}{6\alpha_{s,max}} - \frac{\sqrt{3}\rho_s g_0 \alpha_s \varphi (1 - e_w^2)\theta_s^{3/2}}{4\alpha_{s,max}} \tag{21}$$

where φ and e_w represent the specularity coefficient and particle–wall restitution coefficient, respectively. The value of φ and e_w are adjusted to be between 0.9-0.99 and 0.0001-0.001, respectively, to ensure mass balance for various conditions. The discrepancy of solid distribution and velocity caused by coefficient differences has been proven to be very small.[74]

3.2 | Computational domain and boundary conditions

A symmetric computational domain with the same dimension as the experimental heat sink was used and shown in Figure 5A. To avoid poor quality meshed grids, the geometry was slightly simplified by removing the round angles and pilot holes as given in Figure 5B. The simplification has been numerically proved to barely affect the temperature distribution of the heat sink. The fluid domain and the nearby zone were meshed with tetrahedron grids while the rest solid domain with hexahedron grids. Figure 5C gives a side view of the computational grids on cross-section A. The average mesh size of the fluid domain varies between 0.1 and 0.35 mm for a grid-dependence analysis, and the 0.2 mm mesh size was found to be sufficient for an accurate calculation without consuming too much computational resource. Mesh sizes larger than 0.25 mm was found to result in temperature deviation higher than 3.83% compared to the experimental value thus not recommended. The selected mesh yielded a dimensionless wall distance y + near 1 in the sublayer, and average solid domain size of 0.48 mm. The mesh count was approximately 5 million for the whole solution domain, with 43.19% tetrahedron and 56.81% hexahedron. A periodic meshed fluid domain was given in Figure 5D for easily understand by the readers.

The 3D simulations were conducted using a CFD software under the FLUENT 18.2 (ANSYS Inc.) environment, which employs the Euler-Euler model for two-phase mixtures. The water properties were incorporated as a polynomial function with coefficients listed in Table 2, so does the measured thermosphysical properties of the PCD. The inlet mass flowrate varied from 4 to 10 L/min, and the atmospheric pressure (101 325 Pa) was assigned to the sink outlet. Constant velocity of the two phases (U_{in} = 1.05-2.62 m/s) and solid volume fraction (ϕ = 5-25%) were applied at the heat sink inlet. A uniform heat flux was assigned to the circular heating surface, which ranges from 0.5 to 2.5 kW. The rest walls of the heat sink were set to be adiabatic at the room temperature of 298.15 K. In addition, as mentioned earlier, a no-slip boundary condition was given to the water phase and the Johnson-Jackson partial-slip condition was adopted for the PCM phase at the wall. The governing equations for both fluid and particle phases of the PCD were discretized using the finite-volume method with a second order upwind scheme. The pressure-velocity coupling correlation was solved with the phase-coupled SIMPLE (Semi-Implicit Method for Pressure Lined Equation) algorithm.[75] The time step was selected to be
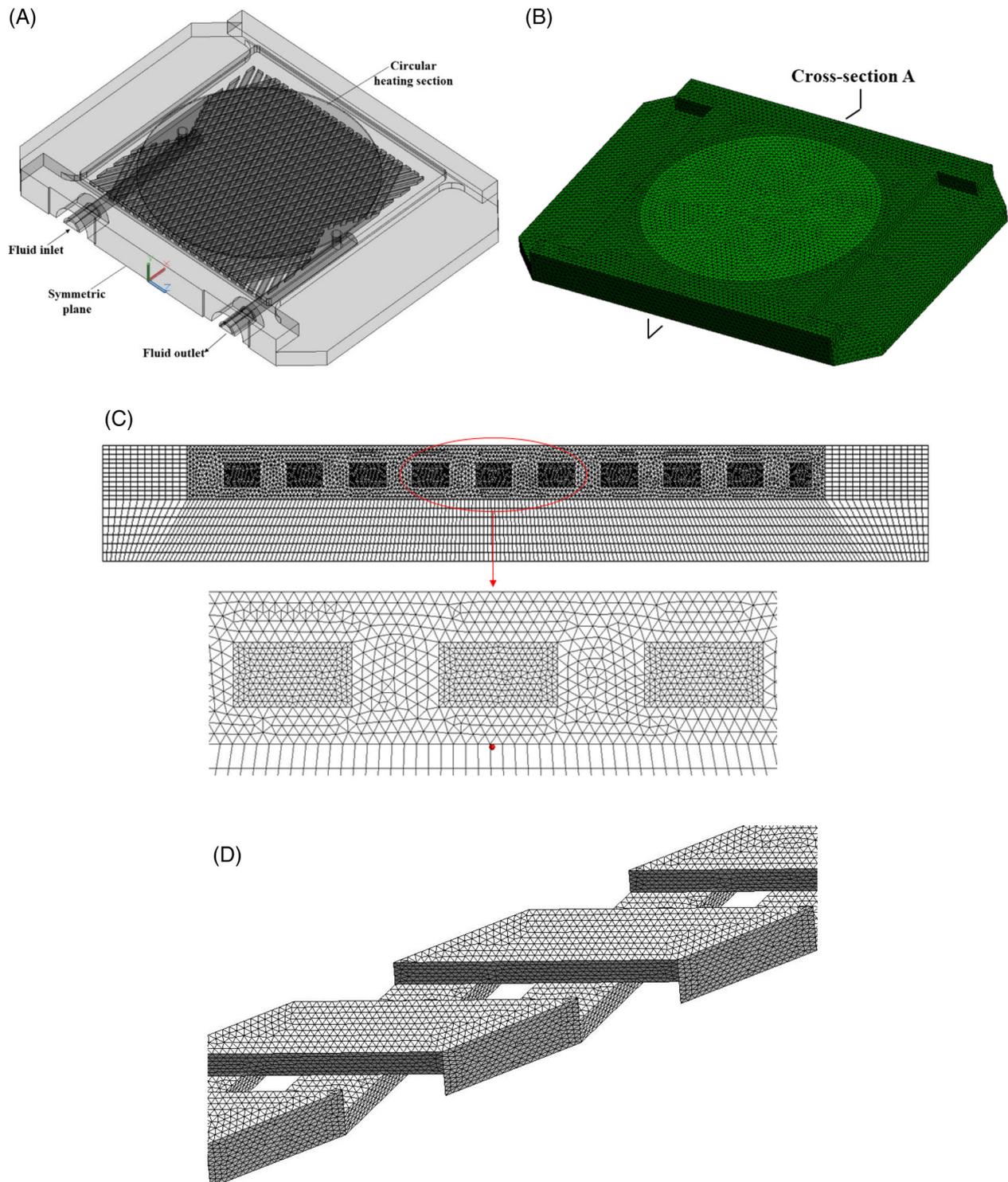
(A)

(B)

(C)

(D)

FIGURE 5 A, Symmetric computational domain and boundaries, B, grid system, C, Side views of computational grids on cross-section A, and D, grid of the a periodic web [Colour figure can be viewed at wileyonlinelibrary.com]

TABLE 2 Thermal and transport properties of water as a function of temperature

$\emptyset$	A_1	A_2	A_3	A_4	A_5
ρ [kg/m³]	1.351E+03	−2.422	6.32E-03	−6.989E-06	-
k [W/(m·K)]	−2.946E-01	4.757E-03	−5.712E-06	-	-
c_p [J/(kg·K)]	6.515E+01	−6.166E-01	2.299E-03	−3.755E-06	2.276E-09
μ [kg/(m·s)]	3.738E-02	−3.093E-04	9.609E-07	−1.320E-09	6.746E-13

Note: $\emptyset(T) = A_1 + A_2T + A_3T^2 + A_4T^3 + A_5T^4$ with T in Kelvin.

0.0001 second and the convergence criterion was set to be 10^{-4} for all variables.

4 | RESULTS AND DISCUSSION

4.1 | Pressure drop comparison between PCD and water

Figure 6A compares the pressure drop of water and PCD derived from both experiment and simulation for Q = 1-14 L/min. Inlet temperature of 313.15 K and 333.15 K are tested for water. The discrepancy of experimental pressure drop caused by inlet temperature is small, with an average deviation of 5.82% under all flow rates. One can see that the Euler-Euler model agrees well with experimental measurements within 6.12%. A change in the particle size (1-7 μm) barely influences the pressure drop (deviation within 0.11%), thus the medium particle size, $\bar{d} = 3.5$ μm, was employed for the rest simulations. It is noteworthy that although the viscosity of PCD can be 10 times that of water during phase change, the pressure drop only increased by 17.01% on average under the studied conditions. Chen et al.[32] showed a PCD ($\bar{d} = 51$ μm, 30 wt. %) pressure drop increase by up to 35.71% in a straight pipe with the viscosity of the PCD 5.57 times that of water. Similarly Alvarado et al.[33] proved that the increased pressure caused by PCD barely affected the pumping work even though the viscosity was 3.5 times higher than water.

To evaluate the Fanning friction $f_{Fanning}$ and the pumping power P_{pump}, the following equations are used:

- Averaged Fanning friction factor

$$f_{Fanning} = \frac{2\Delta P D_{hyd} \sin\alpha}{N\rho_{avg,fluid} U_{avg}^2 W} \tag{22}$$
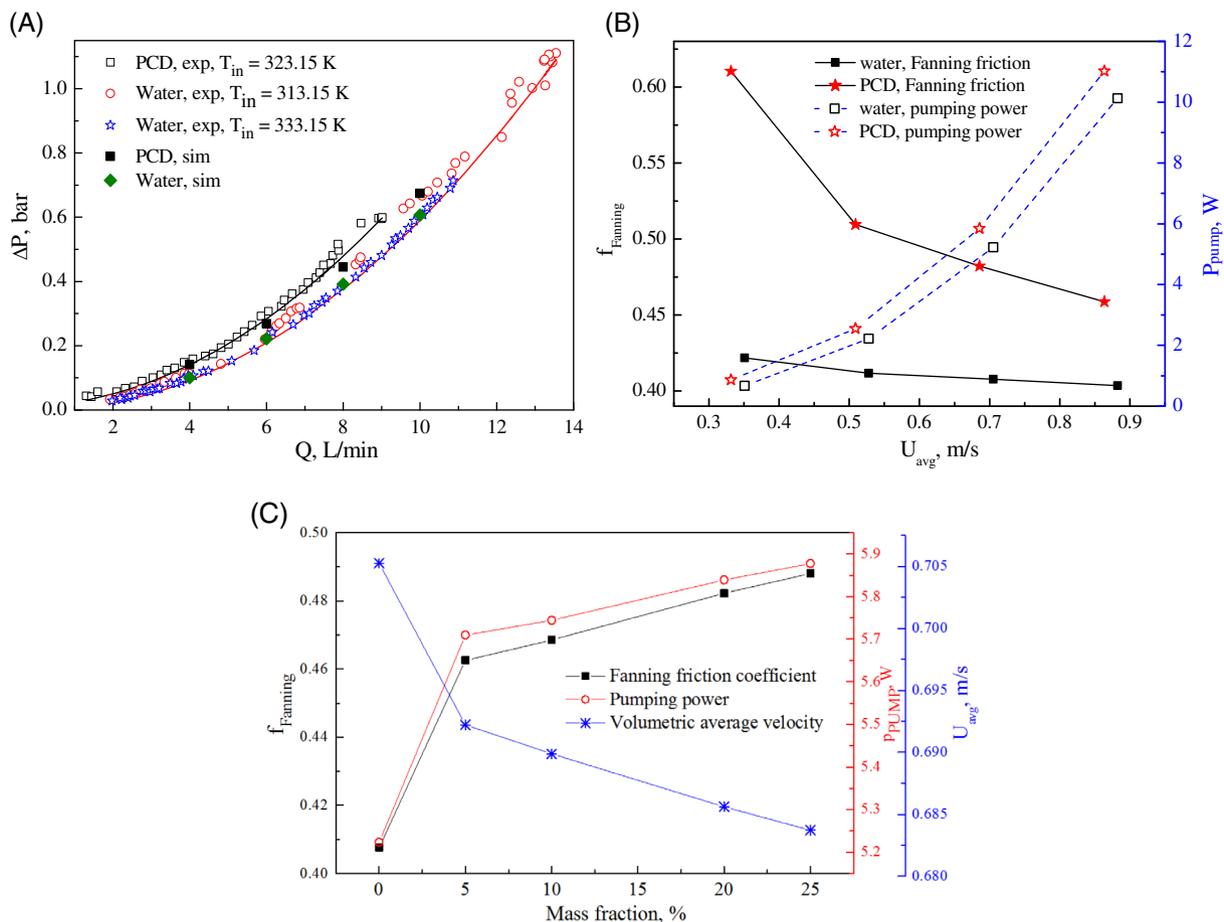
- Pumping power

FIGURE 6 A, Experimental and numerical pressure drop as a function of flow rate for water and PCD, Q = 4, 6, 8, 10 L/min; B, Fanning friction factor and pumping power as a function of flow rate, Q = 4, 6, 8, 10 L/min, P = 1.1 kW; C, Pumping power, fanning friction and volumetric average velocity as a function of PCM mass fraction, Q = 8 L/min and P = 1.1 kW [Colour figure can be viewed at wileyonlinelibrary.com]

$$P_{pump} = \frac{m_f \Delta P}{\rho_{avg,fluid}} \qquad (23)$$

where D_{hyd} is the hydraulic diameter of channel; $\rho_{avg,fluid}$ and U_{avg} represent the volumetric-averaged fluid density and velocity, respectively; N is the channel number of the two-layer web; W is the width of cooling section and α is the angle of web against the side wall (75°). D_{hyd} in Equation (22) is defined by the channel height ($H_c = 4.0$ mm) and width ($W_c = 3.6$ mm) as:

$$D_{hyd} = \frac{4A}{P} = \frac{2H_C W_c}{H_C + W_c} \qquad (24)$$

and $\rho_{avg, fluid}$ and U_{avg} are given respectively by:

$$U_{fluid,avg} = \frac{\int_1^n U_i dv_i}{\int_0^n dv_i} \qquad (25)$$

$$\rho_{fluid,avg} = \frac{\int_0^n \rho_{fluid,i} dv_i}{\int_0^n dv_i} \qquad (26)$$

Figure 6B plots the $f_{Fanning}$ and P_{pump} against the volumetric-averaged velocity at Q = 4-10 L/min. The inlet velocity under such mass flowrate range varies within 1.05-2.62 m/s, which is markedly higher than the U_{avg} (0.35-0.89 m/s). The U_{avg} of the PCD is smaller than that of water by 3.04% on average, due to higher viscosity as discussed earlier. Compared to water, the $f_{Fanning}$ of the PCD shows a steeper decreasing trend with an average value of 19.40% higher than that of water. Additionally, PCD requires a higher pumping power than that of water (by 16.19% on average), especially at a high U_{avg}.

The effect of PCM mass fraction on pressure performance is also evaluated under Q = 8 L/min, as given in Figure 6C. Both the $f_{Fanning}$ and P_{pump} increase with the growth of mass fraction. Taken $f_{Fanning}$ as an example, the increment is 13.47% from $\phi = 0$ to $\phi = 5\%$ but

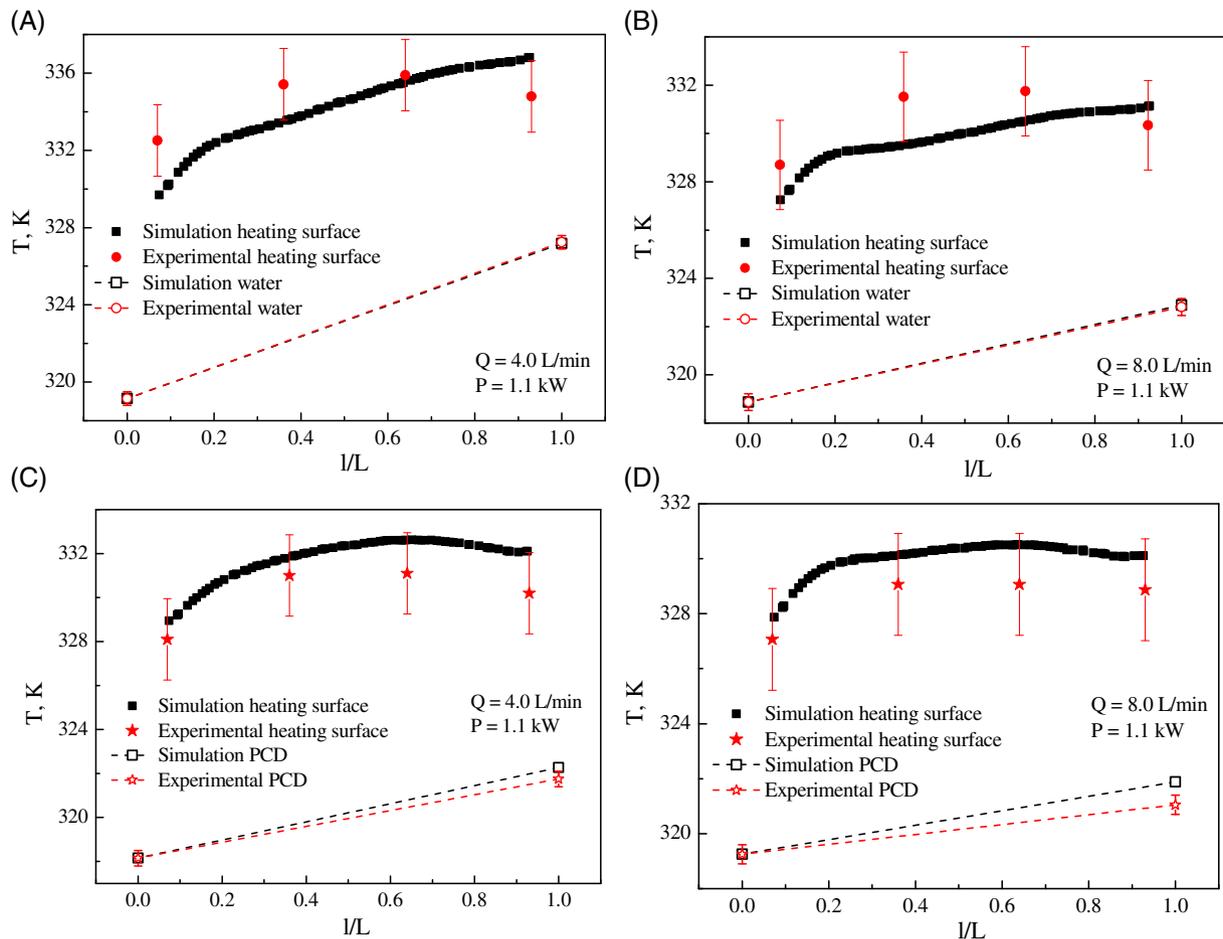**FIGURE 7** Comparison of water temperature on the heating surface and fluid from experiment and simulation, A, Q = 4 L/min, P = 1.1 kW; B, Q = 8 L/min, P = 1.1 kW; Comparison of PCD temperature on the heating wall and fluid from experiment and simulation, C, Q = 4 L/min, P = 1.1 kW; D, Q = 8 L/min, P = 1.1 kW [Colour figure can be viewed at wileyonlinelibrary.com]

becomes 5.52% from $\phi = 5\%$ to $\phi = 25\%$. The decreasing U_{avg} at high mass fraction attributed to the increasing PCD viscosity. However, the influence of PCM concentration on U_{avg} is very limited as the growth is only 3.05% from $\phi = 0$ to $\phi = 25\%$.

4.2 | Temperature comparison between PCM and water

Both the measurement uncertainty (± 0.35 K) and thermal resistance (3.628×10^{-3} K/W $< R_{th} < 6.268 \times 10^{-3}$ K/W) are considered when analysing the temperature heating sink. On Figure 11, the temperatures of heating surface and fluid are plotted against dimensionless distance, which is defined as the ratio of distance from inlet centre and length of cooling section (L = 118 mm). The experimental heating surface represents the temperature directly derived from copper block, and the deviation caused by thermal resistance and temperature uncertainty is ± 1.82 K for $P = 1.1$ kW. Under flow rates of Q = 4 and 8 L/min (shown in Figure 7A and B), the numerical water temperatures of the inlet and outlet are almost identical to experiment measurement. The fluid temperature difference ($\Delta T_{fluid} = T_{out} - T_{in}$) decreases markedly with the increasing flow rate, from 8.09 K at Q = 4 L/min to 3.94 K at Q = 8 L/min. On the heating surface, high temperature are spotted near the outlet side from simulation while the experiment found it near the centre. The difference may be attributed to the non-uniform temperature distribution of six heating cartridges in the copper block. Nevertheless, the simulation predictions fall into the range of experimental measurement. The surface temperature of
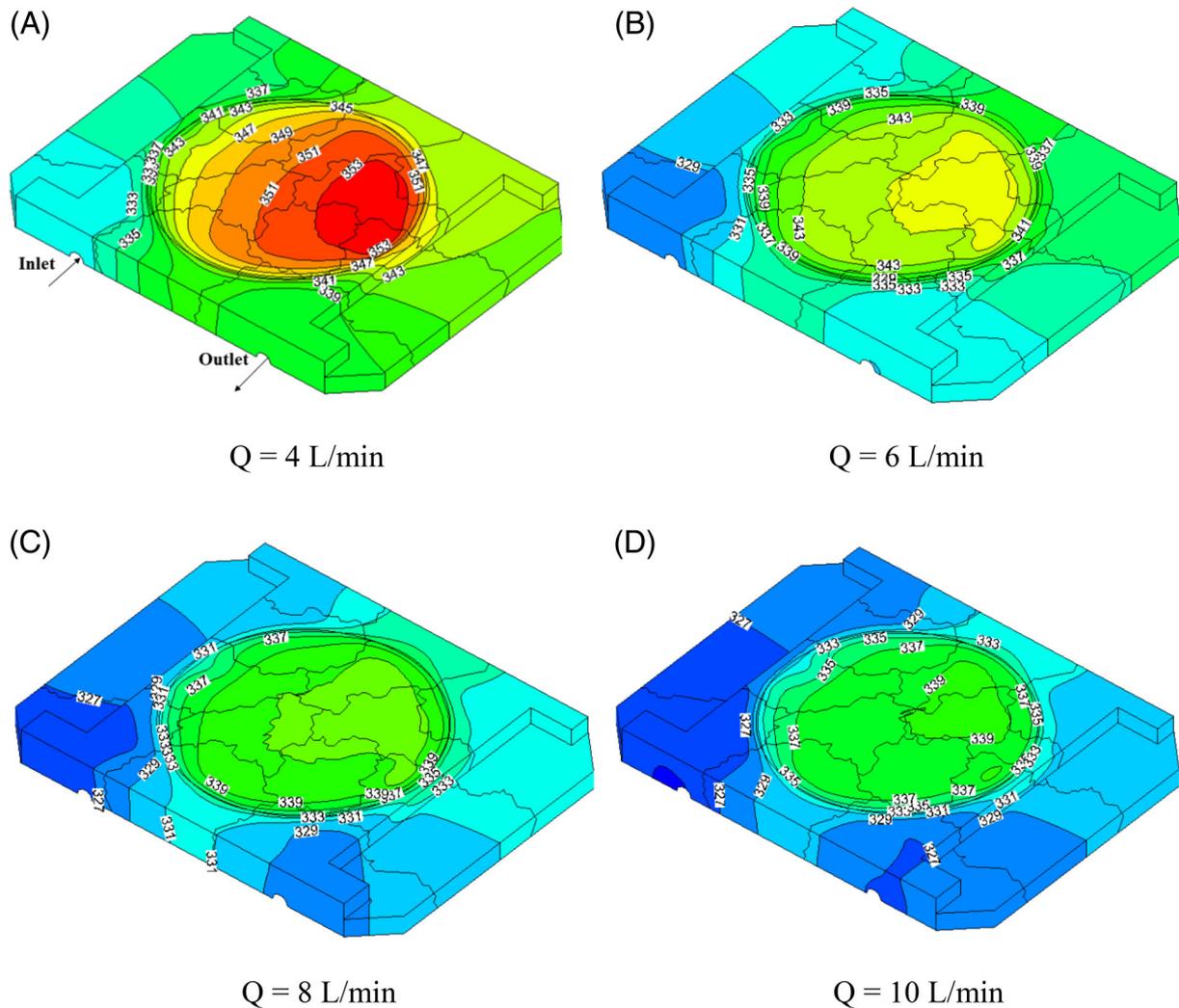

FIGURE 8 Comparison of temperature distribution on the heat sink surface under various PCD flow rates with A, Q = 4 L/min, B, Q = 6 L/min, C, Q = 8 L/min and D, Q = 10 L/min at the conditions of $P = 2.2$ kW, $\phi = 20\%$ and T = 325-353 K [Colour figure can be viewed at wileyonlinelibrary.com]

Q = 4 L/min is significantly higher than that of Q = 8 L/min under the same P, by 4.37 K on average from simulation. The discrepancies of heat sink and fluid temperatures caused by different PCM particle sizes (1-7 μm) are very small (less than ±0.05 K), and the medium particle size $\bar{d} = 3.5$ μm will be used for the following thermal analysis.

Similar comparison are also conducted for PCD at Q = 4 and 8 L/min and P = 1.1 kW, as shown in Figure 7C and D. The outlet fluid temperature from simulation is slightly lower than the experiment measurements, by 0.8 K at Q = 8 L/min. The ΔT_{fluid} of PCD decreases from 3.6 K at Q = 4 L/min to 1.8 K at Q = 8 L/min. The predicted surface temperature follows the trend of experiment, with the highest temperature located nearly ¼ L distance from outlet. The average surface temperature of Q = 8 L/min is 1.73 K lower than that of Q = 4 L/min. Overall, the proposed model yields accurate results in terms of pressure and temperature, and the hydro- and thermo-dynamic

features of PCD can now be confidently studied using the Euler-Euler model.

4.3 | Parameters influences of PCD

Having verified the confidence of numerical model, the influences of flow rate, heating flux and PCM fraction on heat transfer as well as the overall performance were discussed in detail. The inlet temperature of PCD was chosen just below the PCM solidus point and kept at $T_{in} = 320.15$ K. Figure 8 shows the 3D temperature distribution of the heat sink surface under various PCD flow rates (Q = 4-10 L/min), where PCD was pumped into the heat sink from left entrance. High temperature can always be spotted near the outlet region on the heating surface. The highest surface temperature at Q = 4 L/min reaches 353 K but decreases to 339 K at Q = 10 L/min, and a more evenly distributed temperature surface is obtained at high flow rate. The uniform temperature
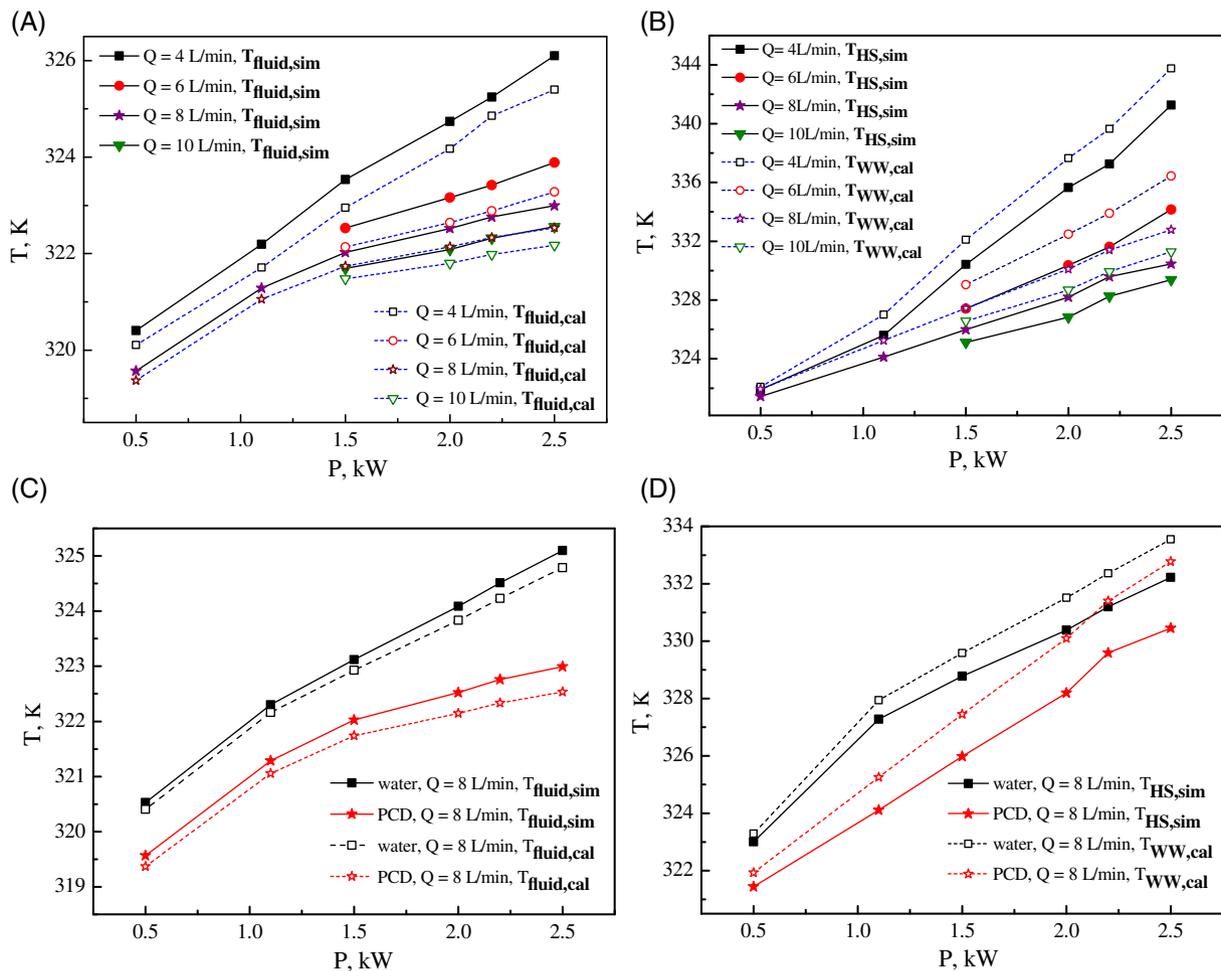

FIGURE 9 Temperature of PCD A, and HS B, from simulation and calculation, Q = 4-10 L/min, P = 0.5-2.5 kW, φ = 20%; C, volumetric-averaged fluid temperature; D, volumetric-averaged heat sink and wetting wall from simulation at Q = 8 L/min, P = 0.5-2.5 kW, φ = 20% [Colour figure can be viewed at wileyonlinelibrary.com]

guarantees the safety working condition of sensitive HVDC converter components. Large temperature gradient can be observed at the surrounding area of heating surface, reaching temperature difference of 6 K within 2-3 mm. Similarly, the temperature on other walls of the heat sink decrease with the growth of flow rates. The non-uniformity of the heat sink temperature, defined as $\theta = \frac{(T_{HS,max} - T_{HS,min})}{q}$, yields $\theta = 1.3e\text{-}04$ at $Q = 4$ L/min and $\theta = 7.8e\text{-}05$ at $Q = 10$ L/min. The low non-uniformity presents a more evenly distributed temperature field inside the heat sink.

The volumetric-averaged fluid/solid temperature can be directly determined by $T_{fluid,sim} = \frac{\int_0^n T_i dv_i}{\int_0^N dv_i}$ from simulation. However, it is difficult to measure the value from experiment and the connection between $T_{fluid,\,sim}$ and T_{in}/T_{out} is unclarified for the heat sink with complex geometry. Figure 9A compares the PCD $T_{fluid,\,sim}$ and calculated temperature, $T_{fluid,cal} = \frac{T_{in} + T_{out}}{2}$, under different flow rates and heating powers. Overall, high heat power P and low flow rate Q favour the growth of PCD

temperature. The $T_{fluid,\,cal}$ shows the same trend of $T_{fluid,\,sim}$, with average deviation of 0.828%.

The temperature of average wetted wall ($T_{WW,cal}$), which refers to the liquid-solid coupled surface, is employed to calculate the heat sink temperature[36,76] and given as

$$T_{WW,cal} = T_{HS,surf} - R_{cond\,HS}Q \quad (27)$$

where the 1D thermal conduction resistance of the heat sink is calculated as

$$R_{cond\,HS} = \frac{H_{HS}}{k_{HS}A_{HS}}$$
$$= \frac{0.032\,m}{185\,W/mK \cdot (3.14 \times 0.0675 \times 0.0675)m^2} = 0.0121\frac{K}{W} \quad (28)$$

where H_{HS} is the average distance between the heating surface and wetted wall and $T_{HS,\,surf}$ is the average temperature of the heating surface. Figure 9B shows the
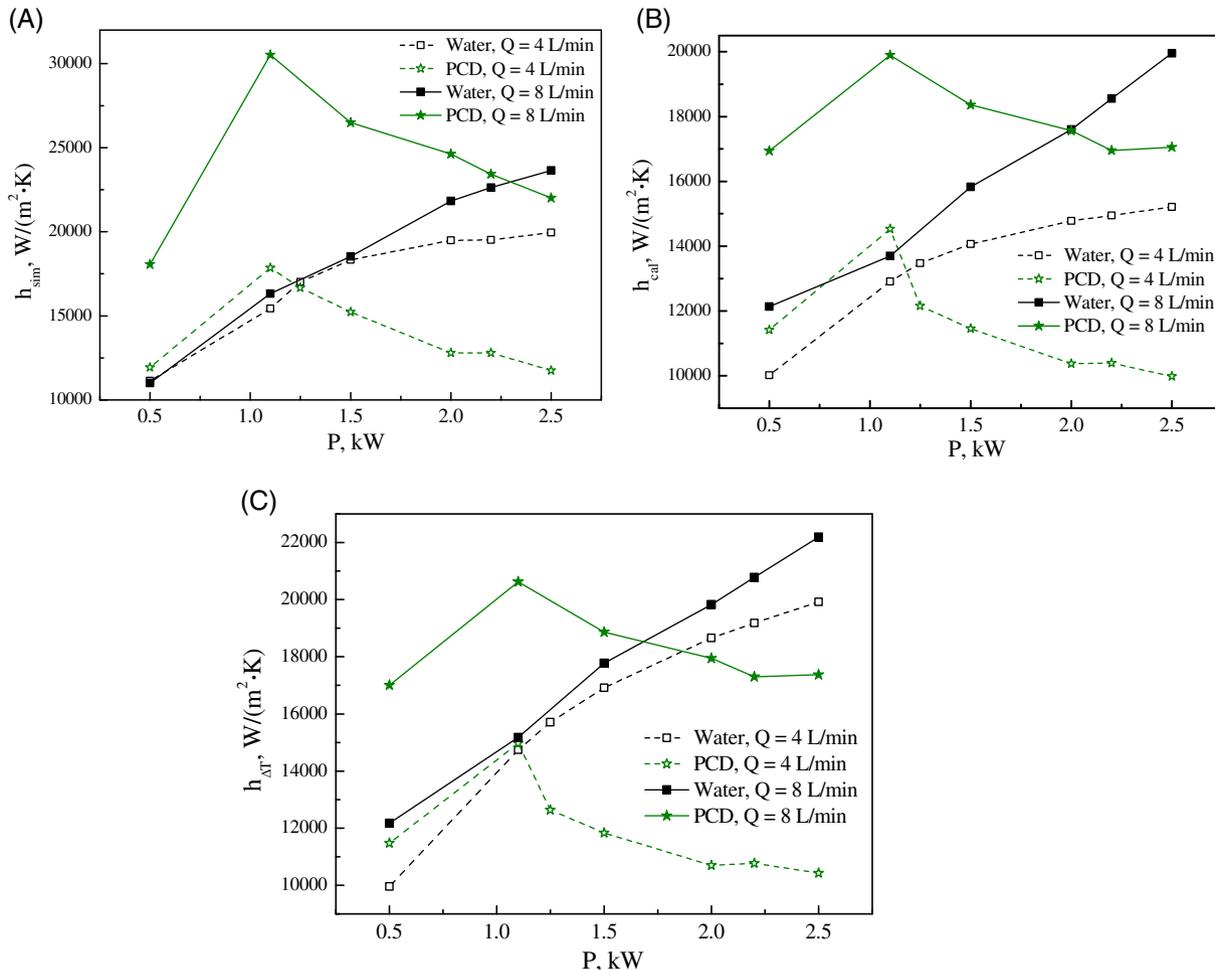

FIGURE 10 Heat transfer coefficient using three calculation methods for Q = 4 and 8 L/min, P = 0.5-2.5 kW, φ = 20% [Colour figure can be viewed at wileyonlinelibrary.com]

volumetric-averaged heat sink temperature of $T_{HS,sim}$ and $T_{WW,cal}$ under the same condition of fluid. Similarly, higher heat sink temperature can be found at high P and low Q. The $T_{WW,cal}$ is slightly higher than that of $T_{HS,sim}$ by 1.55% on average. As a result, the temperature of fluid ($T_{fluid, cal}$) and heat sink ($T_{WW,cal}$) derived from outlet and heating surface respectively can be used to evaluate the thermal performance.

Figure 9C compare the temperature of fluid and heat sink for water and PCD under the same condition. The temperature of water is higher than that of PCD by 1.42 K for $T_{fluid, sim}$ and 1.53 K for $T_{fluid, cal}$. The temp difference between water and PCD is more obvious at high heating power, reaching 2.25 K at $P = 2.5$ kW for $T_{fluid, cal}$. It is attributed to the latent heat absorption of fatty acid ester, which introduces a more isothermal fluid environment for the cooling process. Compared to the fluid, the heat sink temp difference between water and PCD is slight larger, with average value of 2.18 K for $T_{HS,sim}$ and 1.55 K for $T_{WW,cal}$. Therefore, the cooling performance of

PCD is better due to the lower fluid and heat sink temperature under the same heat dissipation from HVDC converter.

When it comes to evaluate the thermal performance using heat transfer coefficient ($h = q/\Delta T$), various temp differences (ΔT) driving the convective heat transfer are employed. It is noteworthy that small deviation of ΔT may result in large oscillation of h under high heat flux, leading to a contrary analysis of water and PCD. To ensure reliability of the evaluation, three calculation methods of heat transfer coefficient are compared: h_{sim} based on volumetric-averaged temperature, h_{cal} from temperature of wetted wall and fluid inlet/outlet and $h_{\Delta T}$ based on log mean temp difference:

$$h_{sim} = \frac{q}{T_{HS,sim} - T_{fluid,sim}} \tag{29}$$

$$h_{cal} = \frac{q}{T_{WW,cal} - T_{fluid,cal}} \tag{30}$$
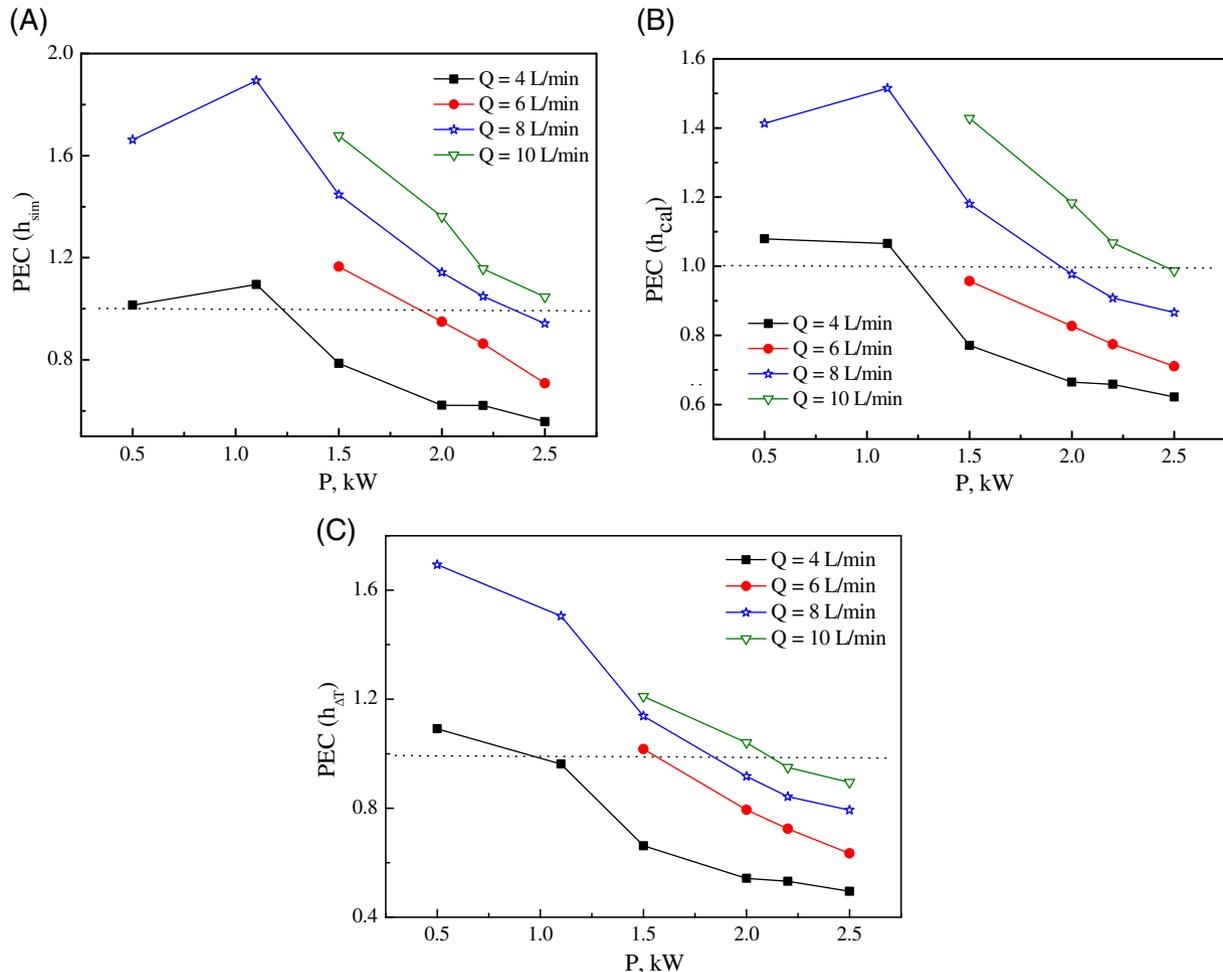
FIGURE 11 PEC comparison using three calculation methods for Q = 4-10 L/min, P = 0.5-2.5 kW, and ϕ = 20% [Colour figure can be viewed at wileyonlinelibrary.com]
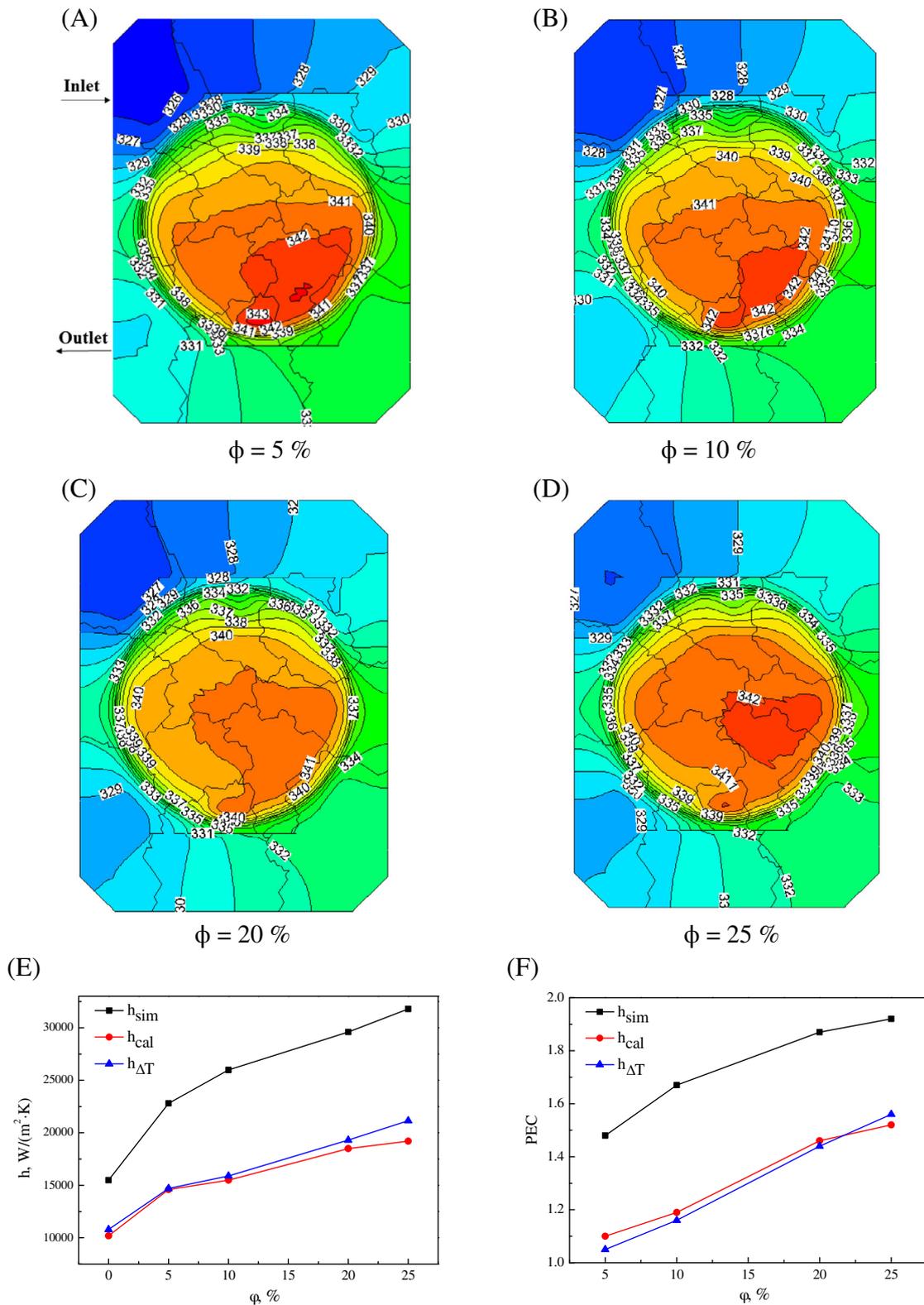
FIGURE 12 Comparison of temperature distribution on the heating surface under various PCM mass fraction with A, 5%, B, 10%, C, 20% and D, 25% at the conditions of Q = 8 L/min, P = 2.2 kW, T = 326-343 K; E, heat transfer coefficient and F, PEC as a function of mass fraction at the conditions of Q = 8 L/min and HF = 1.1 kW [Colour figure can be viewed at wileyonlinelibrary.com]

$$\Delta T = \frac{T_{fluid,out} - T_{fluid,in}}{\ln\left(\frac{T - T_{fluid,in}}{T_{HS,avg} - T_{fluid,out}}\right)}, h_{\Delta T} = \frac{q}{\Delta T} \quad (31)$$

where $T_{HS,\,avg}$ is the average temperature of the heating surface. Using expressions (30) and (31), the measured temperatures of heating surface and fluid inlet/outlet can be integrated for thermal evaluation. Figure 10 compares the heat transfer coefficients of water and PCD using the three methods. The volumetric-averaged temperature always yields a higher value (h_{sim}) than the other two methods for both fluids. Increasing Q favours the growth of heat transfer coefficient for water. Under a given Q, the heat transfer coefficient of water shows a nearly linear increasing relationship of heating power P. However, a peak can be spotted at $P = 1.1$ kW for PCD, and the maximum value increases with increasing Q. For $P < 1.1$ kW, PCD shows better cooling performance than water especially at high Q. Exceeding this point, the heat transfer coefficient of PCD decreases until lower than that water, which implies that the working condition is no longer favourable. The corresponding P of intersection point between water and PCD at $Q = 8$ L/min is $P = 2.25$ kW for h_{sim}, but becomes $P = 1.63$ kW for $h_{\Delta T}$. The favorable working condition of PCD is narrower at low Q, and the cooling performance of PCD is always worse than that of water at $Q = 4$ L/min for $h_{\Delta T}$.

The advantage of PCD is resulted from the latent heat of PCM, but the influence of latent heat reduces when large transport heat applied, where sensible heat becomes dominated. Thus, the superiority of PCD over water is more apparent at small heating power. Meanwhile, the high fluid temperature caused by low Q is beyond the latent heat range. For example, $T_{fluid,\,sim}$ reaches 326 K at $Q = 4$ L/min for $P = 2.5$ kW, but decreases to 322 K at $Q = 10$ L/min under the same condition. The Cp of PCD at 322 K is nearly 7000 J/(kg K) but only around 4000 J/(kg K) at 326 K. Therefore, the thermal performance of PCD may be worse than that of water at low flow rates.

In order to evaluate the heat transfer enhancement and pressure drop penalty, a performance evaluation criteria (PEC) proposed by Webb[77] was used:

$$PEC = \frac{Nu_{p,avg}/Nu_{w,avg}}{\left(f_{p,avg}/f_{w,avg}\right)^{1/3}} \quad (32)$$

where Nu_w and f_w refers to the Nusselt number and friction factor of water, and the averaged Nu number can be calculated based heat transfer coefficient:

$$Nu_{avg} = \frac{h_{avg}D_{hyd}}{\lambda_{Tmean,fluid}} \quad (33)$$

A comparison of PEC using the three calculation methods are given in Figure 11. The trend predicted by h_{sim} and h_{cal} is very similar but the overall PEC based on h_{sim} is larger. Thus, a wider application range where PCD behaves better than water (PEC > 1) is derived by h_{sim}. The maximum PEC can be obtained at $P = 1.1$ kW under all flowrates, due to the thermal enhancement. The influence of flow rates on PEC predicted from h_{cal} is less significant than that of h_{sim}. For example, PEC (h_{sim}) and PEC (h_{cal}) are almost identical at $Q = 4$ L/min, but the difference of the two PECs may reach upto 24.98% at $Q = 8$ L/min. The peak of PEC ($h_{\Delta T}$) can be found at a lower heating power $P = 0.5$ kW, because the thermal enhancement could not offset the pressure drop penalty at $P = 1.1$ kW with this method. It is understandable because the h_{sim} increased by 68.99% from $P = 0.5$ kW to $P = 1.1$ kW at $Q = 8$ L/min, while the increment is only 21.30% for $h_{\Delta T}$. Considering the representativeness of h_{sim} as a volumetric-averaged parameter, the h_{cal} method is recommended for future experimental evaluation due to small deviation.

To clarify the influence of PCM mass fraction on thermal performance, the 2D temperature distribution from a top view are compared under $\phi = 5$-25% as given in Figure 12A-D. The PCD enters the heat sink from top left and leaves at a higher temperature on the bottom left. Higher temperature can still be detected on the heating surface near outlet side, but no remarkable improvement can be observed under all ϕ. The average heating surface temperature of $\phi = 5\%$ is higher than that of $\phi = 25\%$ by 0.71 K.

A quantitative analysis of heat transfer coefficient and PEC under different PCM mass fractions is given in Figure 12E and F. The thermal transfer performance improves with the increasing of PCM concentration. The highest heat transfer coefficient can be found at $\phi = 25\%$, which is around 1.42 times of water regardless of the calculation method. Taken pressure drop penalty into consideration, the best performance can still be observed at the highest PCD concentration, because the enhanced thermal transfer is able to offset the increased pressure drop caused by PCM particles. The PEC results from h_{cal} and $h_{\Delta T}$ are very close, but lower than that of h_{sim} by 29.88% on average. As a conclusion, the best working condition of the developed fatty acid ester-based PCD is $Q = 8$ L/min, $P = 1.1$ kW and $\phi = 25\%$ under the present study range.

5 | CONCLUSIONS

The work detailed in this paper concerns with a high-performance cooling method for a HVDC converter using

fatty acid ester-based phase change dispersion (PCD) in a heat sink with double-layer oblique-crossed ribs. Both experimental investigation and numerical modelling were performed and the following conclusions are obtained:

1. Although the viscosity of the PCD was several times higher than that of water, the increased pumping power was only 17.01% on average. An addition of a small amount of PCM particles significantly increased the friction factor from $\phi = 0\%$ to 5%, but the extent of the increase reduced with further increase in the ϕ from 5% to 25%.

2. The temperature of both heat sink and fluid under water cooling were higher than that of PCD under the same set of working conditions, due to the latent heat of the PCM. Thus, the PCD could achieve a safer and cooler environment for sensitive HVDC converter components like IGBT.

3. The h_{sim} method based on volumetric-averaged temperature yielded a larger value than the other two calculation methods, which were derived from temperatures of heating surface, wetted wall and fluid inlet/outlet. The thermal performance of PCD was only enhanced at a suitable working range, where heating power, fluid flowrate and PCM concentrations all played important roles. For all three methods, a peak of heat transfer coefficient can be observed at $P = 1.1$ kW, where average fluid temperature was more close to PCM melting temperature and higher C_p presented. Increasing fluid flowrate favoured the growth of heat transfer coefficient.

4. Considering the fact that the operational condition of industrial heat exchange is usually at turbulent flow regime, the PCD is greatly competitive than water as energy transport HTF. An optimal set of working conditions was proposed and a flowrate of 8 L/min under a heating power of 1.1 kW and a PCM concentration of 25% was recommended for industrial cooling operations. Moreover, the h_{cal} method was recommended to evaluate the heat sink with complex cross-distributed multilayer channel, using experimental measurable temperature of $T_{WW, cal}$ and $T_{fluid, cal}$.

ACKNOWLEDGEMENTS

NOMENCLATURE

A	heating area, (m^2)
C_D	drag force coefficient
C_L	lift coefficient
c_p	specific heat capacity, (kJ/kg K)
C_{td}	dispersion coefficient
d	droplet size, (μm)
D_{hyd}	hydraulic diameter, (m)
e_{ss}	particle–particle restitution coefficient
e_w	particle–wall restitution coefficient
f	average fanning friction factor
F	force, (N)
g_0	radial distribution function
h	heat transfer coefficient, (W/m^2 K)
h_{sl}	particle–liquid heat transfer coefficient, (W/m^2 K)
H	height, (m)
k	thermal conductivity, (W/m K)
k_{θ_s}	diffusion coefficient
Δh	latent heat, (kJ/kg)
n	size distribution parameter
P	heating power, (W)
P_{el}	electrical power, (W)
P_s	pressure, (Pa)
q_{sw}	Johnson–Jackson fluctuating energy
Q	volume flow rate, (L/min)
R	thermal resistance, (K/W)
s	distance, (m)
T	temperature, (K)
$\vec{v}$	velocity vector, (m/s)
U_{avg}	average velocity, (m/s)
W	width, (m)
Y_d	cumulative volume fraction

GREEK SYMBOLS
α volume concentration
γ shear rate, (s^{-1})
ζ bulk viscosity, (kg/[m s])
θ_s granular temperature, (K)
μ shear viscosity, (kg/[m s])
ρ density, (kg/m^3)
τ stress-strain tensor
Υ collisional dissipation of energy
φ specularity coefficient
Φ volume fraction
ω uncertainty parameter

SUBSCRIPTS

AC	alternating current
DC	direct current
HVDC	high voltage direct current
IGBT	insulated gate bipolar transistor
l	liquid phase
PCD	phase change dispersion
PCM	phase change material
s	solid phase

SST   shear stress transport

ORCID

Qi Li 🔟 https://orcid.org/0000-0002-8209-6637

REFERENCES

1. Giampieri A, Ma Z, Ling Chin J, et al. Techno-economic analysis of the thermal energy saving options for high-voltage direct current interconnectors. *Appl Energy*. 2019;247:60-77.
2. Gomis-Bellmunt O, Junyent-Ferré A, Sumper A, Galceran-Arellano S. Maximum generation power evaluation of variable frequency offshore wind farms when connected to a single power converter. *Appl Energy*. 2010;87:3103-3109.
3. Kabalyk Y. Determination of energy loss in power voltage inverters for power supply of locomotive traction motors. *Procedia Eng*. 2016;165:1437-1443.
4. Lips HP. Technology trends for HVDC thyristor valves. POWERCON '98 1998 International Conference on Power System Technology Proceedings (Cat No98EX151); vol 1; August 18-21,1998; Beijing, China:451-455.
5. Wang P, McCluskey P, Bar-Cohen A. Hybrid solid- and liquid-cooling solution for Isothermalization of insulated gate bipolar transistor power electronic devices. *IEEE Trans Compon Packag Manuf Technol*. 2013;3:601-611.
6. Guo Y-f, Ma X-l, Shi P. Power losses and temperature variations in a power converter for an electronic power steering system considering steering profiles. *J Instrum Technol*. 2014;2: 40-46.
7. Kang SS. Advanced cooling for power electronics. Paper presented at: 2012 7th International Conference on Integrated Power Electronics Systems (CIPS); March 6-8,2012; Nuremberg, Germany:1-8.
8. Wrzecionko B, Biela J, Kolar JW. SiC power semiconductors in HEVs: influence of junction temperature on power density, chip utilization and efficiency. Paper presented at: 2009 35th Annual Conference of IEEE Industrial Electronics; November 3-5,2009; Porto, Portugal:3834-3841.
9. Huang AQ. Power semiconductor devices for smart grid and renewable energy systems. *Proc IEEE*. 2017;105:2019-2047.
10. Haack J, Akyol B, Tenney N, Carpenter B, Pratt R, Carroll T. VOLTTRON™: an agent platform for integrating electric vehicles and Smart Grid. Paper presented at: 2013 International Conference on Connected Vehicles and Expo (ICCVE); December 2-6,2013; Las Vegas, NV:81-86.
11. Faschang M, Cejka S, Stefan M, et al. Provisioning, deployment, and operation of smart grid applications on substation level. *Comput Sci Res Develop*. 2017;32:117-130.
12. Drofenik U. Theoretical converter power density limits for forced convection cooling. *Proceedings of the International PCIM Europe Conference*. 2005;2005:608-619.
13. Kandlikar SG, Hayner CN. Liquid cooled cold plates for industrial high-power electronic devices—thermal design and manufacturing considerations. *Heat Transf Eng*. 2009;30:918-930.
14. Ali HM. Recent advancements in PV cooling and efficiency enhancement integrating phase change materials based systems-a comprehensive review. *Sol Energy*. 2020;197:163-198.

15. Ali H, Abdul W. Qasim Muhammad Arslan, Janjua Muhammad Mansoor, Ali Muhammad Aon, Ali hafiz Muhammad, Jadoon Tufail Rehman, Ali Ejaz, Raza Ahsan, Javaid Noshairwan. Thermal management and uniform temperature regulation of photovoltaic modules using hybrid phase change materials-nanofluids system. *Renew Energy*. 2020;145:282-293.
16. Li C, Li Q, Ding Y. Investigation on the thermal performance of a high temperature packed bed thermal energy storage system containing carbonate salt based composite phase change materials. *Appl Energy*. 2019;247:374-388.
17. Li C, Li Q, Li Y, et al. Heat transfer of composite phase change material modules containing a eutectic carbonate salt for medium and high temperature thermal energy storage applications. *Appl Energy*. 2019;238:1074-1083.
18. Li C, Li Q, Ding Y. Investigation on the effective thermal conductivity of carbonate salt based composite phase change materials for medium and high temperature thermal energy storage. *Energy*. 2019;176:728-741.
19. Pu L, Xu L, Zhang S, Li Y. Optimization of ground heat exchanger using microencapsulated phase change material slurry based on tree-shaped structure. *Appl Energy*. 2019;240: 860-869.
20. Ma F, Zhang P, Shi XJ. Investigation of thermo-fluidic performance of phase change material slurry and energy transport characteristics. *Appl Energy*. 2018;227:643-654.
21. Chen J, Zhang P. Preparation and characterization of nano-sized phase change emulsions as thermal energy storage and transport media. *Appl Energy*. 2017;190:868-879.
22. Wang F, Zhang C, Liu J, Fang X, Zhang Z. Highly stable graphite nanoparticle-dispersed phase change emulsions with little supercooling and high thermal conductivity for cold energy storage. *Appl Energy*. 2017;188:97-106.
23. Lankveld JMG, Lyklema J. Adsorption of polyvinyl alcohol on the paraffin—water interface. III emulsification of paraffin in aqueous solutions of polyvinyl alcohol and the properties of paraffin-in-water emulsions stabilized by polyvinyl alcohol. *J Colloid Interface Sci*. 1972;41:475-483.
24. Jin Z, Wang Y, Liu J, Yang Z. Synthesis and properties of paraffin capsules as phase change materials. *Polymer*. 2008;49:2903-2910.
25. Xin X, Zhang H, Xu G, Tan Y, Zhang J, Lv X. Influence of CTAB and SDS on the properties of oil-in-water nano-emulsion with paraffin and span 20/tween 20. *Colloids Surf A Physicochem Eng Asp*. 2013;418:60-67.
26. Shchukina E, Graham M, Zheng Z, Shchukin D. Nanoencapsulation of phase change materials for advanced thermal energy storage systems. *Chem Soc Rev*. 2018;47:4156-4175.
27. Noël JA, Kahwaji S, Desgrosseilliers L, Groulx D, White MA. Chapter 13 - phase change materials. In: Letcher TM, ed. *Storing Energy*. Oxford, UK: Elsevier; 2016:249-272.
28. Hasan A, Hejase H, Abdelbaqi S, Assi A, Hamdan M. Comparative effectiveness of different phase change materials to improve cooling performance of heat sinks for electronic devices. *Appl Sci*. 2016;6:226.
29. Shah RK, London AL. *Laminar Flow Forced Convection in Ducts: A Source Book for Compact Heat Exchanger Analytical Data*. Cambridge, Massachusetts: Academic Press; 2014.

30. Huang L, Petermann M. An experimental study on rheological behaviors of paraffin/water phase change emulsion. *Int J Heat Mass Transfer*. 2015;83:479-486.

31. Pollerberg C, Doetsch C. Phase Changing Slurries in cooling and cold supply networks. Paper presented at: 10th International Symposium on District Heating and Cooling; September 3-5, 2006; Oberhausen, Germany.

32. Chen B, Wang X, Zhang Y, Xu H, Yang R. Experimental research on laminar flow performance of phase change emulsion. *Appl Therm Eng*. 2006;26:1238-1245.

33. Alvarado JL, Marsh C, Sohn C, Phetteplace G, Newell T. Thermal performance of microencapsulated phase change material slurry in turbulent flow under constant heat flux. *Int J Heat Mass Transfer*. 2007;50:1938-1952.

34. Rao Y, Dammel F, Stephan P, Lin G. Flow frictional characteristics of microencapsulated phase change material suspensions flowing through rectangular minichannels. *Sci China Ser E: Technol Sci*. 2006;49:445-456.

35. Mahmoud S, Tang A, Toh C, Raya A-D, Soo SL. Experimental investigation of inserts configurations and PCM type on the thermal performance of PCM based heat sinks. *Appl Energy*. 2013;112:1349-1356.

36. Kanargi B, Lee PS, Yap C. A numerical and experimental investigation of heat transfer and fluid flow characteristics of an air-cooled oblique-finned heat sink. *Int J Heat Mass Transfer*. 2018;116:393-416.

37. Li WQ, Qu ZG, He YL, Tao WQ. Experimental and numerical studies on melting phase change heat transfer in open-cell metallic foams filled with paraffin. *Appl Therm Eng*. 2012;37:1-9.

38. Chai L, Xia GD, Wang HS. Numerical study of laminar flow and heat transfer in microchannel heat sink with offset ribs on sidewalls. *Appl Therm Eng*. 2016;92:32-41.

39. Kanargi OB, Lee PS, Yap C. A numerical and experimental investigation of heat transfer and fluid flow characteristics of a cross-connected alternating converging–diverging channel heat sink. *Int J Heat Mass Transfer*. 2017;106:449-464.

40. Remeljej CW, Hoadley AFA. An exergy analysis of small-scale liquefied natural gas (LNG) liquefaction processes. *Energy*. 2006;31:2005-2019.

41. Moein P, Sarmad M, Ebrahimi H, Zare M, Pakseresht S, Vakili SZ. APCI- LNG single mixed refrigerant process for natural gas liquefaction cycle: analysis and optimization. *J Nat Gas Sci Eng*. 2015;26:470-479.

42. Wang Z, Li Y. Layer pattern thermal design and optimization for multistream plate-fin heat exchangers—a review. *Renew Sustain Energy Rev*. 2016;53:500-514.

43. Radwan A, Ookawara S, Ahmed M. Thermal management of concentrator photovoltaic systems using two-phase flow boiling in double-layer microchannel heat sinks. *Appl Energy*. 2019;241:404-419.

44. Alhuyi Nazari M, Ahmadi MH, Ghasempour R, et al. A review on pulsating heat pipes: from solar to cryogenic applications. *Appl Energy*. 2018;222:475-484.

45. Srikanth R, Nemani P, Balaji C. Multi-objective geometric optimization of a PCM based matrix type composite heat sink. *Appl Energy*. 2015;156:703-714.

46. Coleman B, Ostanek J, Heinzel J. Reducing cell-to-cell spacing for large-format lithium ion battery modules with aluminum or PCM heat sinks under failure conditions. *Appl Energy*. 2016;180:14-26.

47. Yüncü H. Thermal contact conductance of nominaly flat surfaces. *Heat Mass Transfer*. 2006;43:1-5.

48. Shi L, Wu G, Wang H-L, Yu X-M. Interfacial thermal contact resistance between aluminum nitride and copper at cryogenic temperature. *Heat Mass Transfer*. 2012;48:999-1004.

49. Fletcher L, Gyorog D. *Heat Transfer Between Surfaces in Contact: An Analytical and Experimental Study of Thermal Contact Resistance of Metallic Interfaces*. Mechanical Engineering Department, Arizona State University, Tempe, Arizona, United States. 1971.

50. Göktepe S, Atalık K, Ertürk H. Comparison of single and two-phase models for nanofluid convection at the entrance of a uniformly heated tube. *Int J Therm Sci*. 2014;80:83-92.

51. Wang J, Wang S, Zhang T, Liang Y. Numerical investigation of ice slurry isothermal flow in various pipes. *Int J Refrig*. 2013;36:70-80.

52. Xi W, Cai J, Huai X. Numerical investigation on fluid-solid coupled heat transfer with variable properties in cross-wavy channels using half-wall thickness multi-periodic boundary conditions. *Int J Heat Mass Transfer*. 2018;122:1040-1052.

53. Fischer L, Maranda S, Stamatiou A, von Arx S, Worlitschek J. Experimental investigation on heat transfer with a phase change dispersion. *Appl Therm Eng*. 2019;147:61-73.

54. Rajabifar B. Enhancement of the performance of a double layered microchannel heatsink using PCM slurry and nanofluid coolants. *Int J Heat Mass Transfer*. 2015;88:627-635.

55. Chiu C-P, Maveety JG, Tran QA. Characterization of solder interfaces using laser flash metrology. *Microelectron Reliab*. 2002;42:93-100.

56. Xiao X, Zhang G, Ding Y, Wen D. Rheological characteristics of molten salt seeded with Al2O3 Nanopowder and graphene for concentrated solar power. *Energies*. 2019;12:467.

57. Muñoz-Sánchez B, Nieto-Maestre J, Veca E, et al. Rheology of solar-salt based nanofluids for concentrated solar power. Influence of the salt purity, nanoparticle concentration, temperature and rheometer geometry. *Sol Energy Mater Sol Cells*. 2018;176:357-373.

58. Itoh T, Wanibe Y. Derivation of number based size distribution from modified mass based rosin-Rammler distribution and estimation of the various mean particle diameters of powder. *Trans Jpn Inst Met*. 1988;29:671-684.

59. Herrmann-Heber R, Reinecke SF, Hampel U. Dynamic aeration for improved oxygen mass transfer in the wastewater treatment process. *Chem Eng J*. 2019;122068. https://doi.org/10.1016/j.cej.2019.122068

60. Bordet A, Poncet S, Poirier M, Galanis N. Advanced numerical modeling of turbulent ice slurry flows in a straight pipe. *Int J Therm Sci*. 2018;127:294-311.

61. Menter F. Zonal two equation kw turbulence models for aerodynamic flows. Paper presented at: 23rd Fluid Dynamics, Plasma dynamics, and Lasers Conference; July 6-9, 1993; Orlando, FL:2906.

62. Lun C, Savage SB, Jeffrey D, Chepurniy N. Kinetic theories for granular flow: inelastic particles in Couette flow and slightly inelastic particles in a general flowfield. *J Fluid Mech*. 1984;140:223-256.

63. Syamlal M, O'Brien T. Computer simulation of bubbles in a fluidized bed. *AIChe Symp Ser*. 1989;85:22-31.

64. Ogawa S, Umemura A, Oshima N. On the equations of fully fluidized granular materials. *Z Angew Math Phys*. 1980;31:483-493.

65. Kitanovski A, Poredoš A. Concentration distribution and viscosity of ice-slurry in heterogeneous flow. *Int J Refrig*. 2002;25:827-835.

66. Gidaspow D. *Multiphase Flow and Fluidization: Continuum and Kinetic Theory Descriptions*. Cambridge, Massachusetts: Academic Press; 1994.

67. Pu W, Zhao C, Xiong Y, et al. Numerical simulation on dense phase pneumatic conveying of pulverized coal in horizontal pipe at high pressure. *Chem Eng Sci*. 2010;65:2500-2512.

68. Saffman PG. The lift on a small sphere in a slow shear flow. *J Fluid Mech*. 2006;22:385-400.

69. Simonin C, Viollet P. Predictions of an oxygen droplet pulverization in a compressible subsonic coflowing hydrogen flow. *Num Method Multiph Flows*. 1990;91:65-82.

70. Gunn DJ. Transfer of heat or mass to particles in fixed and fluidised beds. *Int J Heat Mass Transfer*. 1978;21:467-476.

71. Zehner P, Schlünder EU. Wärmeleitfähigkeit von Schüttungen bei mäßigen Temperaturen. *Chem Ing Tech*. 1970;42:933-941.

72. Legawiec B, Ziólkowski D. Structure, voidage and effective thermal conductivity of solids within near-wall region of beds packed with spherical pellets in tubes. *Chem Eng Sci*. 1994;49:2513-2520.

73. Johnson PC, Jackson R. Frictional–collisional constitutive relations for granular materials, with application to plane shearing. *J Fluid Mech*. 1987;176:67-93.

74. Jiang YY, Zhang P. Numerical investigation of slush nitrogen flow in a horizontal pipe. *Chem Eng Sci*. 2012;73:169-180.

75. Patankar S. *Numerical Heat Transfer and Fluid Flow*. Boca Raton, Florida: CRC Press; 1980.

76. Hu S, McFarland AR. Numerical performance simulation of a wetted wall bioaerosol sampling cyclone. *Aerosol Sci Tech*. 2007;41:160-168.

77. Webb RL. Performance evaluation criteria for use of enhanced heat transfer surfaces in heat exchanger design. *Int J Heat Mass Transfer*. 1981;24:715-726.